PCCP

RSC Publishing

PAPER

View Article Online
View Journal | View Issue

Cite this: *Phys. Chem. Chem. Phys.*, 2013, **15**, 13538

CO_2 capture properties of lithium silicates with different ratios of Li_2O/SiO_2: an *ab initio* thermodynamic and experimental approach†

Yuhua Duan,*[a] Heriberto Pfeiffer,[b] Bingyun Li,[ac] Issis C. Romero-Ibarra,[b] Dan C. Sorescu,[a] David R. Luebke[a] and J. Woods Halley[d]

Received 18th April 2013,
Accepted 5th June 2013

DOI: 10.1039/c3cp51659h

www.rsc.org/pccp

The lithium silicates have attracted scientific interest due to their potential use as high-temperature sorbents for CO_2 capture. The electronic properties and thermodynamic stabilities of lithium silicates with different Li_2O/SiO_2 ratios (Li_2O, Li_8SiO_6, Li_4SiO_4, $Li_6Si_2O_7$, Li_2SiO_3, $Li_2Si_2O_5$, $Li_2Si_3O_7$, and α-SiO_2) have been investigated by combining first-principles density functional theory with lattice phonon dynamics. All these lithium silicates examined are insulators with band-gaps larger than 4.5 eV. By decreasing the Li_2O/SiO_2 ratio, the first valence bandwidth of the corresponding lithium silicate increases. Additionally, by decreasing the Li_2O/SiO_2 ratio, the vibrational frequencies of the corresponding lithium silicates shift to higher frequencies. Based on the calculated energetic information, their CO_2 absorption capabilities were extensively analyzed through thermodynamic investigations on these absorption reactions. We found that by increasing the Li_2O/SiO_2 ratio when going from $Li_2Si_3O_7$ to Li_8SiO_6, the corresponding lithium silicates have higher CO_2 capture capacity, higher turnover temperatures and heats of reaction, and require higher energy inputs for regeneration. Based on our experimentally measured isotherms of the CO_2 chemisorption by lithium silicates, we found that the CO_2 capture reactions are two-stage processes: (1) a superficial reaction to form the external shell composed of Li_2CO_3 and a metal oxide or lithium silicate secondary phase and (2) lithium diffusion from bulk to the surface with a simultaneous diffusion of CO_2 into the shell to continue the CO_2 chemisorption process. The second stage is the rate determining step for the capture process. By changing the mixing ratio of Li_2O and SiO_2, we can obtain different lithium silicate solids which exhibit different thermodynamic behaviors. Based on our results, three mixing scenarios are discussed to provide general guidelines for designing new CO_2 sorbents to fit practical needs.

1. Introduction

During the past few decades, lithium silicates and zirconates have been extensively investigated as CO_2 sorbents in an attempt to alleviate the consequences of global warming.[1–30] Nakagawa and Ohashi[12,13] reported a novel method to capture CO_2 from high-temperature gases through the reversible reaction of $Li_2ZrO_3 + CO_2 \leftrightarrow ZrO_2 + Li_2CO_3$. Later, a similar reaction mechanism $Li_4SiO_4 + CO_2 \leftrightarrow Li_2SiO_3 + Li_2CO_3$ was reported for the Li_4SiO_4 case.[7,8,11,16–19] It has been found that Li_4SiO_4 maintains its CO_2 absorption effectiveness during cycling between absorption at 973 K and regeneration at 1123 K in the case of pure CO_2 at a total pressure of 1.0×10^5 Pa.[4,7] Following this pioneering work, several other studies have been published on the possibility of using lithium ceramics to separate CO_2 and N_2. Venegas *et al.*[17] pointed out that Li_2SiO_3 could further react with CO_2 through the reaction $Li_2SiO_3 + CO_2 \leftrightarrow SiO_2 + Li_2CO_3$ and in doing so make Li_4SiO_4 a more efficient sorbent. Kato *et al.*[7,8] compared Li_4SiO_4 with Li_2ZrO_3 and found that at 500 °C and in an atmosphere containing 20% CO_2 gas, the weight increase of Li_4SiO_4 was about 50% greater than that

[a] *National Energy Technology Laboratory, United States Department of Energy, 236 Cochrans Mill Road, Pittsburgh, Pennsylvania 15236, USA. E-mail: yuhua.duan@netl.doe.gov; Fax: +1 412-386-5990; Tel: +1 412-386-5771*
[b] *Instituto de Investigaciones en Materiales, Universidad Nacional Autónoma de México, Circuito Exterior s/n, Cd Universitaria, Del. Coyoacan, CP 04510, México DF, Mexico*
[c] *School of Medicine, West Virginia University, Morgantown, West Virginia 26506, USA*
[d] *School of Physics and Astronomy, University of Minnesota, Minneapolis, Minnesota 55455, USA*

† Electronic supplementary information (ESI) available. See DOI: 10.1039/c3cp51659h

of Li_2ZrO_3. Additionally, Li_4SiO_4 was found to absorb CO_2 more than 30 times faster than Li_2ZrO_3. Sodium-based oxides have also been used either as low-temperature ($T < 250$ °C) CO_2 sorbents or as promoters for lithium-based acceptors. Lopez-Ortiz *et al.*[9] reported the use of Na-based sorbents at high temperatures as an alternative to lithium-based CO_2 sorbents, and their results showed that Na-ceramics are able to capture CO_2 at 600 °C and are candidates to compete with Li_4SiO_4 and Li_2ZrO_3. Essaki *et al.*[2–4] concluded that the CO_2 absorption properties of Li_4SiO_4 pellets are strongly affected by the absorption temperature. Between 550 °C and 600 °C, Li_4SiO_4 shows the most rapid CO_2 absorption. Above 600 °C, it absorbs only a very small amount of CO_2. Gauer and Heschel[5] as well as Ortiz-Landeros and coworkers[31] demonstrated that doping in Li_4SiO_4 with vacancies or hetero elements can enhance its CO_2 absorption at moderate temperature. Venegas *et al.*[17] investigated the effect of particle size upon CO_2 absorption by Li_4SiO_4 and found that this may influence the stability of the Li_4SiO_4 particles during the CO_2 sorption–desorption cycles, and lithium sublimation as Li_2O takes place on small particles. Yamaguchi *et al.*[19] made Li_4SiO_4 membranes from powders and performed measurements of CO_2 separation. Using such membranes, they obtained a separation factor of 5.5 for CO_2 and N_2 at a temperature of 525 °C. Using thermogravimetric analysis (TGA), Okumura *et al.*[14] investigated CO_2 absorption in Li_4SiO_4 and found that it corresponds to a pseudo first order reaction. They estimated activation energies of about 115 kJ mol^{-1} in the 620–660 °C region and about 56 kJ mol^{-1} in the 680–700 °C region. The large differences among these activation energies were associated with the different surface states of the Li_4SiO_4 particle. Olivares-Marin *et al.*[15] investigated Li_4SiO_4-based sorbents made from fly ashes for CO_2 capture at high temperature. Recently, Durán-Muñoz *et al.*[32] explored the CO_2 capture properties of a high lithium-content silicate (Li_8SiO_6) and found that it could absorb CO_2 over a wide range of temperatures and has a maximum capacity of 11.8 mmol CO_2 per gram of Li_8SiO_6. They also found that its CO_2 capture mechanism depends on the reaction temperature.

To date, the mechanisms of these reversible reactions for lithium silicates capturing CO_2 are still unclear. Essaki *et al.*[4] proposed a reaction model for CO_2 absorption by lithium silicate at room temperature. In the model, the CO_2 reacts with Li_2O in Li_4SiO_4 to form Li_2CO_3. If H_2O is also present, CO_2 and Li_2O will first hydrolyze, and then form Li_2CO_3. Recently, Rodriguez-Mosqueda and Pfeiffer[16] evaluated the CO_2 chemisorption capacity of Li_4SiO_4 as a function of CO_2 flow rate and sorbent particle size. Their results showed that at low CO_2 flows CO_2 capture is controlled by CO_2 diffusion through the gas-film system, whereas at high CO_2 flows it is controlled by the CO_2 chemisorption reaction rate. After formation of the carbonate-oxide external shell, the whole CO_2 capture process is controlled kinetically by lithium diffusion. However, they failed to explain how CO_2 diffuses into the shell and the Li_2O (in the form of Li^+ and O^{2-}) diffuses out of Li_4SiO_4 to further form carbonate. Mosqueda *et al.*[10] investigated the chemical sorption of CO_2 on Li_2O and found that in order to continue to form Li_2CO_3,

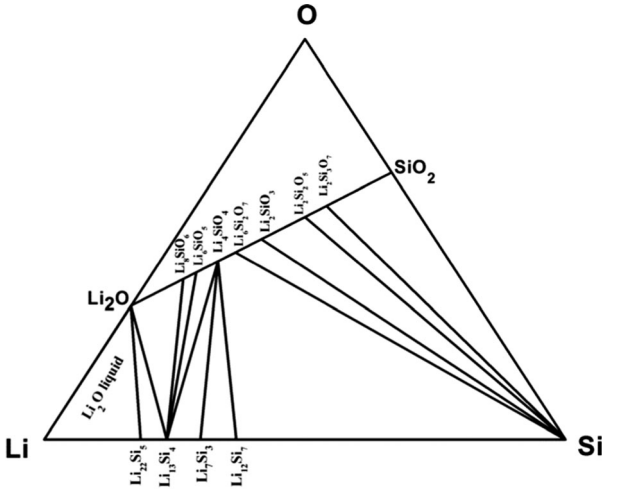

Fig. 1 Illustrative phase diagram of the ternary system Li–Si–O at high temperatures (>700 K) obtained based on data in ref. 33–36.

the lithium has to migrate and cross the Li_2CO_3 shell. Such diffusion is topochemical and is promoted by temperature. A similar double shell model was also used to describe the Li_2ZrO_3 sorbent.[6,18] However, to date it is not yet known how the Li_4SiO_4 structure is changed upon CO_2 absorption to form Li_2CO_3 with Li_2SiO_3 or SiO_2 and how the Li_2O component of Li_4SiO_4 is extracted and reacts with CO_2. Cruz *et al.*[1] analyzed the thermal decomposition of Li_4SiO_4 and Li_2SiO_3. By lithium sublimation, Li_4SiO_4 begins to decompose between 900 and 1000 °C, while Li_2SiO_3 was highly stable. However, the nature of the intermediates involved in this structural transformation is not clear. Actually, from the phase diagram of the Li_2O–SiO_2 binary system made by Kracek,[35] it can be seen that different lithium silicate compositions can be formed as a function of SiO_2 percentage and the external temperature. Such a phase diagram corresponding to the Li–Si–O system at high temperature is summarized in Fig. 1.[33–36] Based on Kracek's work, Claus *et al.*[36] investigated the phase equilibria in the Li_4SiO_4–Li_2SiO_3 region of the pseudo binary Li_2O–SiO_2 system at temperatures between 1000 and 1300 °C. Above 1000 °C, with increasing percentage of SiO_2, as shown in Fig. 1, several different lithium silicate phases can exist, *e.g.* Li_8SiO_6, Li_4SiO_4, $Li_6Si_2O_7$, Li_2SiO_3, $Li_2Si_2O_5$, and $Li_3Si_2O_7$. Between Li_8SiO_6 and Li_4SiO_4, and between $Li_2Si_2O_5$ and SiO_2, there are also a number of meta-stable intermediate phases such as Li_6SiO_5 and $Li_2Si_3O_7$.[33,34,37] Obviously, $Li_6Si_2O_7$ could be one of the intermediates between Li_4SiO_4 and Li_2SiO_3 as it could be formed through the transition reaction $Li_6Si_2O_7 \leftrightarrow Li_4SiO_4 + Li_2SiO_3$.

In the literature there are only limited theoretical studies on the electronic structures of crystalline lithium silicates. By employing an orthogonalized linear combination of atomic orbitals method (OLCAO), Ching *et al.*[38] calculated the electronic structures of Li_2SiO_3 and $Li_2Si_2O_5$ and compared them with XPS measurements. Their results showed that the effective charge on Li is quite small (0.07 in Li_2SiO_3, and 0.02 in $Li_2Si_2O_5$). With an *ab initio* approach, Uchino and Yoko[39,40] investigated the local coordination environments of the alkali cations (Li^+ and Na^+) in

the cluster model of single- and mixed-alkali silicate glasses. Their results demonstrated that the average coordination number of alkali cations increased from Li to Na and each alkali cation is located in individual local sites in both single- and mixed-alkali clusters. Munakata and Yokoyama[41] calculated the electronic structure of Li_4SiO_4 and obtained a band gap of 17.5 eV. Du and Corrales[42–44] employed density functional theory to characterize the structural and electronic properties of alkali silicate glasses (M_2O, M = Li, Na, K), Li_2SiO_3, and $Li_2Si_2O_5$. Their results revealed that there are clear differences in the band structure corresponding to the bridging and non-bridging oxygen ions. To the best of our knowledge no theoretical analysis of the electronic properties of Li_8SiO_6 and $Li_6Si_2O_7$ has been reported to date. In our previous studies,[23,30,45] we have investigated the structural, electronic and thermodynamic properties of Li_2O and Li_2CO_3 and the reaction of $Li_2O + CO_2 \leftrightarrow Li_2CO_3$, and concluded that although Li_2O is efficient to absorb CO_2, by comparison with other lithium salts (such as Li_4SiO_4, Li_2ZrO_3, *etc.*) it is still not a good CO_2 sorbent due to the large energetic requirements involved in the reverse reaction ($Li_2CO_3 \rightarrow Li_2O + CO_2$). We also investigated the thermodynamic properties of two phases of Li_4SiO_4 and found that the thermodynamic properties of these two phases are similar while their optical properties are different.[23] Overall, it was found that the CO_2 capture performances of Li_4SiO_4 are better than those of lithium zirconates.[23]

For these alkali silicates to capture CO_2, their necessary regeneration temperatures are very high (>900 K). Such operating temperatures are outside the normal operating range for pre-combustion CO_2 capture systems, which normally operate at temperatures of 260–500 °C for concurrent water-gas-shift/separation and 40–260 °C for post water-gas-shift separation. Our previous studies already showed that the CO_2 capture temperature of pure Li_2O is higher than the corresponding ones for the silicate (Li_4SiO_4) and zirconate (Li_2ZrO_3).[23,24,30,45] Because the lithium silicates are made by Li_2O and SiO_2, where SiO_2 is a very weak CO_2 sorbent while Li_2O is a strong CO_2 sorbent, it becomes scientifically relevant to analyze the sorption properties of these mixed types of materials. As a result we have conducted further investigations to develop CO_2 sorbents, which could work at the desired operating temperature for pre- or post-combustion CO_2 capture technologies, by mixing weak and strong CO_2 sorbents with different ratios. In this study, we focus on the structural and electronic properties of a series of lithium silicates (Li_8SiO_6, Li_4SiO_4, $Li_6Si_2O_7$, Li_2SiO_3, $Li_2Si_2O_5$, and $Li_2Si_3O_7$) and try to understand the phase evolution $Li_2O \leftrightarrow Li_8SiO_6 \leftrightarrow Li_4SiO_4 \leftrightarrow Li_6Si_2O_7 \leftrightarrow Li_2SiO_3 \leftrightarrow Li_2Si_2O_5 \leftrightarrow Li_2Si_3O_7 \leftrightarrow SiO_2$ by increasing the percentage of SiO_2. Particular attention has been paid to the phase transformations $Li_4SiO_4 \leftrightarrow Li_6Si_2O_7 \leftrightarrow Li_2SiO_3$ and $Li_2SiO_3 \leftrightarrow Li_2Si_2O_5 \leftrightarrow SiO_2$, which are the key structural transformations for the Li_4SiO_4 sorbent during CO_2 sorption–desorption cycles. In contrast to the lithium ion transport problem in a lithium-ion battery, we are interested in the migration mechanism of Li_2O from lithium silicates because the Li_2O (as Li^+ and O^{2-}) group is responsible for the CO_2 absorption process. We want to explore whether, in this series of lithium silicates, optimal compositions can be identified to be used as CO_2 capture sorbents in pre- and/or post-combustion technologies.

This paper is organized as follows: in the next two sections we briefly describe the theoretical method and the experimental measurements we employed, in the fourth section we show our results on these crystals and compare them with other available reports, and in the last section we summarize our conclusions.

2. Theoretical methods

First-principles density-functional theory (DFT) calculations with plane-wave basis sets and pseudopotential approximation were done to describe the structural, energetic and electronic properties of lithium silicates considered in this study. All calculations were performed using the Vienna *ab initio* simulation package (VASP).[46,47] Similar to our previous tests on proper choice of pseudo-potential and exchange–correlation functions for other solid materials,[45,48–50] in this study, we employ the PAW pseudo-potentials and PW91 exchange–correlation functional in all of the calculations. Plane wave basis sets were used with a kinetic energy cutoff of 520 eV and an augmentation charge cutoff of 605.4 eV. The *k*-point sampling grids of $m \times n \times l$, obtained using the Monkhorst–Pack method,[51] were used for these bulk calculations, where m, n, and l were determined with a spacing of about 0.028 $Å^{-1}$ along the reciprocal axes of their unit cells. The corresponding *k*-point sampling grid of each solid is listed in Table 1. The valence electrons contained

Table 1 The experimental crystal structure constants of lithium silicates

Crystal	Lattice constant	Space group and ref.	Li_2O/SiO_2 ratio	*k*-Point grid	f.u.[a]
Li_2O	a = 4.573 Å	$Fm3m$ (no. 225)[66]	1 : 0	8 × 8 × 8	4
Li_8SiO_6	a = 5.4243 Å c = 10.626 Å	$P6_3cm$ (no. 185)[60]	4 : 1	8 × 8 × 4	2
Li_4SiO_4	a = 11.532 Å b = 6.075 Å c = 16.678 Å β = 99.04°	$P2_1/m$ (no. 11)[73]	2 : 1	4 × 6 × 2	14
$Li_6Si_2O_7$	a = 7.71 Å c = 4.88 Å	$P\bar{4}2_1m$ (no. 113)[61]	3 : 2	5 × 5 × 8	2
Li_2SiO_3	a = 9.392 Å b = 5.397 Å c = 4.660 Å	$Cmc2_1$ (no. 36)[62,63]	1 : 1	4 × 8 × 8	4
$Li_2Si_2O_5$	a = 5.82 Å b = 14.66 Å c = 4.79 Å β = 90°	$Ccc2$ (no. 37)[64]	1 : 2	6 × 3 × 8	4
meta-$Li_2Si_2O_5$	a = 5.683 Å b = 4.784 Å c = 14.648 Å	$Pbcn$ (no. 60)[65]	1 : 2	7 × 8 × 3	4
$Li_2Si_3O_7$	a = 19.648 Å b = 5.9969 Å c = 4.8691 Å	$Pmca$ (no. 57)[37]	1 : 3	3 × 7 × 8	4
α-SiO_2	a = 4.8992 Å c = 5.3832 Å γ = 120°	$P3_221$ (no. 154)[72]	0 : 1	8 × 8 × 8	3

[a] The f.u. acronym stands for formula unit.

the s and p orbitals for Li, C, O, and Si atoms. During optimizations all atoms in the cell were allowed to relax. For band structure calculations, the symbols and coordinates of the high symmetrical points in the crystals were taken from Bradley and Cracknell's definitions.[52]

The CO_2 capture reactions of solids can be expressed generically in the form (for convenient description, we normalized the reaction to 1 mole of CO_2)

$$\sum_{R_i} n_{R_i}\ \text{Solid\_R}_i + CO_2 \leftrightarrow \sum_{P_j} n_{P_j}\ \text{Solid\_P}_j \qquad \text{(a)}$$

where n_{R_i}, n_{P_j} are the numbers of moles of reactants (R_i) and products (P_j) involved in the capture reactions. We treat the gas phase CO_2 as an ideal gas. By assuming that the difference between the chemical potentials ($\Delta\mu^0$) of the solid phases of reactants (R_i) and products (P_j) can be approximated by the difference in their total energies (ΔE^{DFT}), obtained directly from DFT calculations, and the vibrational free energy of the phonons and by ignoring the PV contribution terms for solids, the variation of the chemical potential ($\Delta\mu$) for reaction (a) with temperature and pressure can be written as[45,48–50,53,54]

$$\Delta\mu(T,P) = \Delta\mu^0(T) - RT\ln\frac{P_{CO_2}}{P_0} \qquad (1)$$

where

$$\Delta\mu^0(T) \approx \Delta E^{DFT} + \Delta E_{ZP} + \Delta F^{PH}(T) - G^0_{CO_2}(T) \qquad (2)$$

Here, ΔE^{DFT} is the DFT energy difference between the reactants and products of the reaction (a), ΔE_{ZP} is the zero point energy difference between the reactants and products and can be obtained directly from phonon calculations. ΔF^{PH} is the phonon free energy change excluding zero-point energy (which is already counted into the ΔE_{ZP} term) between the solids of products and reactants. P_{CO_2} is the partial pressure of CO_2 in the gas phase and P_0 is the standard state reference pressure taken to be 1 bar. The heat of reaction ($\Delta H^{cal}(T)$) can be evaluated through the following equation:

$$\Delta H^{cal}(T) = \Delta\mu^0(T) + T[\Delta S_{PH}(T) - S_{CO_2}(T)] \qquad (3)$$

where $\Delta S_{PH}(T)$ is the difference of entropies between product solids and reactant solids. The free energy of CO_2 $\left(G^0_{CO_2}\right)$ can be obtained from standard statistical mechanics,[45,49,55] and its entropy (S_{CO_2}) can be found in the empirical thermodynamic databases as follows:[56]

$$G^0_{CO_2}(T) = \frac{7}{2}RT + \sum_{i=1}^{4}\frac{N_a h\nu_i}{e^{\frac{h\nu_i}{kT}} - 1} - TS_{CO_2}(T) \qquad (4)$$

$$S_{CO_2}(T) = A\ln(t) + Bt + C\frac{t^2}{2} + D\frac{t^3}{3} + \frac{E}{2t^2} + G \qquad (5)$$

where N_a is the Avogadro constant, the vibrational frequencies (ν_i) of the CO_2 molecule are 673 cm^{-1} (π_u), 1354 cm^{-1} (σ_g^+), and 2397 cm^{-1} (σ_u^+), from which the zero-point energy of a CO_2 molecule is obtained with a value of 0.316 eV and included in eqn (2),[45,49] $t = T/1000$, and the remaining parameters (A, B, C, D, E, G) can be found from ref. 30 and 56.

The "grand-canonical" Gibbs free energy G' of multi-component systems of all lithium silicates in contact with a CO_2 gas-phase reservoir can be written as (see additional details in the Appendix)[50,55,57,58]

$$G'(T,\mu_g^{CO_2}) = \sum_j^{p-1} x_j F_j(T) - \mu_g^{CO_2}(T,p)\sum_j^{p-1} x_j n_j^c \qquad (6)$$

where $F_j(T)$ is the free energy of the solid phase "j" ($F_j(T) = E^{DFT} + F^{PH}(T)$, ignoring the PV term contribution), p is the number of phases (solid substances and gas phase), x_j is the unknown mole fraction of phase j coexisting at a given composition, temperature, and pressure. The molar fractions x_j are based on elements appearing only as solids and are determined by minimizing the grand-canonical Gibbs free energy, subject to the following mass-conservation constraints for the solid phase species:[57]

$$f_i = \sum_j^{p-1} x_j^{solid} n_i^{j,solid} = \text{constant} \qquad (7)$$

for any element i in a solid except carbon (C in eqn (6)), where f_i is the molar ratio of solid element i and is normalized to obey $\sum_{i=1}^{M} f_i = 1$, $n_i^{j,solid}$ represents the number of atoms of type i in one formula unit of phase j, and M is the number of elements. The minimization of G as given in eqn (6) as a function of x_j and subject to the constraints eqn (7) is a linear programming problem which can be solved using standard techniques.[59] The conditions under which a chemical reaction occurs can be identified by comparing the molar fractions x_j at two consecutive temperature or pressure steps. If the x_j values change then a reaction occurs between the successive temperature or pressure steps. The change in the Gibbs free energy of the system due to a reaction is zero at thermodynamic equilibrium and can be calculated by setting $\Delta\mu(T,P) = 0$ in eqn (1).

3. Experimental

Different thermokinetic analyses and CO_2 chemisorptions were performed using a Q500HR instrument from TA Instruments. Several lithium silicates (Li_8SiO_6, Li_4SiO_4 and Li_2SiO_3, synthesized by solid-state reaction[1,22,31,32]) and lithium oxide (Li_2O, Aldrich) were tested dynamically and isothermally in the presence of a CO_2 flow (Praxair grade 3.0 at 60 mL min^{-1}). Dynamic thermogravimetric analysis (TGA) experiments were performed at 5 °C min^{-1} from 30 to 800 °C, while specific isothermal analyses were performed at 600 °C. To avoid a previous carbonation process, samples were initially heated using a N_2 flow (Praxair grade 4.8, at 60 mL min^{-1}). Thus, once the experimental temperature (600 °C) was reached, the flow gas was switched to CO_2 and the isothermal mass gain experiments were carried out using a CO_2 gas flow.

4. Results and discussions

4.1 Crystalline structures of lithium silicates

According to the phase diagram of the ternary Li–Si–O system illustrated in Fig. 1, one can see that with different Li_2O to SiO_2 ratios, several Li–Si–O crystalline phases can be formed. For Li_2O, the SiO_2/Li_2O ratio is zero and becomes 1.0 for Li_2SiO_3. Li_8SiO_6, Li_4SiO_4, and $Li_6Si_2O_7$ have more Li_2O than SiO_2 as their Li_2O/SiO_2 ratios are greater than 1.0, while $Li_2Si_2O_5$ and $Li_2Si_3O_7$ have more SiO_2 than Li_2O due to their Li_2O/SiO_2 ratios less than 1.0. The crystal structures of these silicates are shown in Fig. 2 and their corresponding experimental crystallographic structural data are summarized in Table 1.

As shown in Fig. 2(a), Li_8SiO_6 has a hexagonal structure with space group $P6_3cm$ (no. 185).[60] As discussed in our previous study,[23] lithium orthosilicate (Li_4SiO_4) usually is found in a monoclinic structure with space group $P2_1/m$ (no. 11), but it also has another phase (γ-Li_4SiO_4) which is in triclinic structure with space group $P\bar{1}$ (no. 2). As shown in Fig. 2(b), the crystal structure of $Li_6Si_2O_7$ is tetragonal with space group $P\bar{4}2_1m$-D_{2d}^3 (no. 113).[61] It belongs to the class of sorosilicates having isolated $[Si_2O_7]$-groups. As shown in Fig. 2(c), lithium catena-silicate (Li_2SiO_3) is in an orthorhombic structure with space group $Cmc2_1$ (no. 36).[62,63] As one can see from Fig. 2(c) in this structure, the tetrahedra form chains parallel to [001] with two tetrahedra in the identity period. Lithium is tetrahedrally coordinated with a mean Li–O distance of 2.0 Å. $Li_2Si_2O_5$ has two kinds of structures as shown in Fig. 2(e) and (f): monoclinic with space group $Ccc2$ (no. 37)[64] and a meta-stable orthorhombic structure with space group $Pbcn$ (no. 60).[65] Very recently, based on single crystal X-ray diffraction Kruger *et al.*[37] determined the structure of $Li_2Si_3O_7$ silicate sheets for which a space group $Pmca$ (no. 57) was found as shown in Fig. 2(g). Under ambient conditions, Li_2O has an antifluorite structure with space group $Fm3m$,[66] and Li_2CO_3 has a monoclinic structure with space group $C2/c$ (no. 15).[67] According to the phase diagram from Fig. 1, the Li_6SiO_5 phase may also exist, but no crystal structure is currently available for this phase. For this reason this phase was not included in the current study. Although SiO_2 exhibits many different crystalline phases under different temperatures and pressures,[68–71] here we only deal with α-quartz, which is the common phase at room-temperature. This phase could exist either as amorphous ($P3_221$, no. 154) or low quartz ($P3_121$, no. 152). Above 573 °C, the α-quartz could transform into β-quartz ($P6_222$, no. 180). Since SiO_2 is involved in our capture reactions, here, we only consider the α-phase of SiO_2 as shown in Fig. 2(d) with the crystallographic parameters taken from ref. 72.

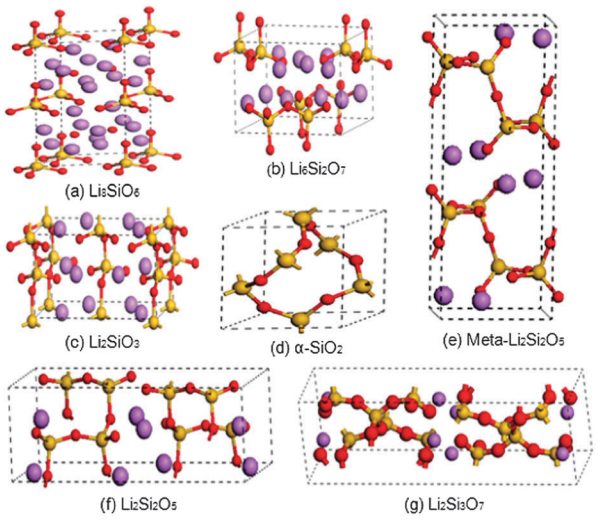

Fig. 2 The crystal structures of lithium silicates. The largest balls (in pink) correspond to Li, the medium size balls (in yellow) stand for silicon while the smallest balls (in red) indicate O atoms. The *c*-axis is taken as the vertical axis for each structure.

These lithium silicates can be synthesized at high temperature with different mixture ratios of Li_2O and SiO_2. Table 1 also lists the Li_2O/SiO_2 molar ratio in each silicate and the number of formula units (f.u.) in their corresponding unit cell. As shown in Fig. 2, the main difference between the metastable $Li_2Si_2O_5$ and the stable form is related to orientation of the silicon oxygen tetrahedra within the silicon oxygen layers. In both Li_8SiO_6 and Li_4SiO_4, the $[SiO_4]$ tetrahedra do not connect directly. Therefore, Li_8SiO_6 can be considered as being composed by two Li_2O units intercalated into Li_4SiO_4. In $Li_2Si_3O_7$, Li_2SiO_3, and $Li_2Si_2O_5$, the $[SiO_4]$ tetrahedra are connected by bridge-oxygen atoms with formation of several $[SiO_4]$ chains. In α-SiO_2, as shown in Fig. 2(d) all $[SiO_4]$ tetrahedra are connected and built into one chain.

The optimized crystal constants of these lithium silicates as determined from our DFT calculations are listed in Table 2. From the table, one can see that the largest deviation from experimental measurements is less than 2%, which indicates that our DFT-based theoretical approach can provide accurate crystallographic parameters for these solids.

Other bulk properties of interest, which we determined by DFT calculations for these solids, are their bulk moduli and cohesive energies. These properties were determined from the dependence of unit cell energy on cell volume by fitting the DFT results to Birch–Murnaghan equation of state.[74,75] The fitted results of these lithium silicates are listed in Table 2. The bulk modulus B is defined as $B = B_0 + B_0' \times P$, where P is the pressure set here to a value of 1 atm. The cohesive energy (E_C) is calculated by subtracting the total bulk energy (E_0 in Table 2) from the sum of spin polarized total energies of the related atoms (such as Li, Si, O) using the same level of calculations (in our case, we get $E_{Li} = -0.04403$ eV, $E_{Si} = -0.12847$ eV, and $E_O = -0.12996$ eV), and then dividing it by the number of formula units in the unit cell (f.u.) shown in Table 1. In Table 2 we indicate the calculated cohesive energies E_C as well as other values reported in the literature.

For comparison, the bulk properties of Li_4SiO_4 and Li_2O from ref. 23 and 45 are also listed in Table 2. From Table 2, it can be seen that overall our fitted parameters and calculated bulk moduli and cohesive energies are in good agreement with the available experimental and theoretical results. From Li_2O to SiO_2, by decreasing the Li_2O/SiO_2 ratio, the bulk modulus

Table 2 The optimized crystal structural constants in Å, the bulk modulus, cohesive energy (E_c), and the fitted parameters of the Birch–Murnaghan equation of state for each lithium silicate and α-SiO_2. The zero-point energy (E_{ZP}) and entropy (S) at T = 300 K from phonon calculations

Crystal	Equilibrium structure and deviations	E_0 (eV per unit cell)	B_0 (eV Å^{-3})	B_0'	Cell volume V_0 (Å^3)	Bulk modulus (GPa)	E_c (eV/f.u.)	E_{ZP} (kJ mol^{-1})	S (J mol^{-1} K^{-1})
Li_2O[a]	a = 4.631(1.3%)	−57.699	0.513	4.074	99.54	82.2	14.207	22.8	44.3
Li_8SiO_6	a = 5.458(0.63%)	−167.303	0.470	4.436	277.38	75.34	82.392	116.9	206.5
	c = 10.710(0.79%)				312.65(exp)[b]				
Li_4SiO_4[c]	a = 11.644(0.97%)	−765.319	0.462	4.328	1197.37	73.94	54.231	71.7	128.7
	b = 6.142(1.10%)								
	c = 16.875(1.18%)				1153.9(exp)[d]				
	β = 99.1°(0.05%)								
$Li_6Si_2O_7$	a = 7.776(0.86%)	−188.221	0.484	4.424	298.52	77.56	92.683	114.9	225.6
	c = 4.910(0.61%)				290.09(exp)[e]				
Li_2SiO_3	a = 9.459(0.71%)		0.454		244.55		39.050	50.4	
	b = 5.441(0.82%)	−158.627		4.699	245.6[f]	72.69			83.2
	c = 4.717(1.23%)	−158.32[f]		5.12[f]	236.2(exp)[g]	72.86[f]			82.0[m]
$Li_2Si_2O_5$	a = 5.881(1.05%)		0.469		423.63		62.611	79.9	126.9
	b = 14.778(0.80%)	−254.424		3.575	408.68(exp)[h]	75.13			
	c = 4.838(0.99%)	−254.08[f]		4.28[f]	424.6[f]	73.04[f]			
meta-$Li_2Si_2O_5$	a = 5.737(0.94%)		0.416		415.18		62.557	79.5	127.4
	b = 4.853(1.45%)	−254.205		4.043	398.52(exp)[i]	66.60			
	c = 14.792(0.98%)	−253.88[f]		4.72[f]	416.0[f]	66.48[f]			
$Li_2Si_3O_7$	a = 19.890(1.23%)	−350.038	0.442	3.783		70.83	86.127	109.5	171.1
	b = 6.055(0.97%)				598.91				
	c = 4.9304(1.26%)				573.70(exp)[j]				
α-SiO_2	a = 5.006(1.88%)	−71.621	0.253	4.168		40.56	23.492	29.2	63.2
	4.9160[k], 4.92[l]			5.99(exp)[k]	119.38	34–37(exp)[k,l]	19.2(exp)[k,l]		
	c = 5.499(1.72%)			(3.1, 4.9)[k]	113.7(exp)[l]	31.3[k]	23.83[k]		
	5.4054[k], 5.412[l]			3.9[l]	107.4[l]	38.1[l]	22.2[l]		

[a] Ref. 45. [b] Ref. 60. [c] Ref. 73. [d] Ref. 23. [e] Ref. 61. [f] Ref. 44. [g] Ref. 62 and 63. [h] Ref. 64. [i] Ref. 65. [j] Ref. 37. [k] Ref. 71. [l] Ref. 70. [m] Ref. 76.

of the corresponding lithium silicate decreases except for $Li_2Si_3O_7$. For Li_2SiO_3 and two phases of $Li_2Si_2O_5$, our calculated results are very close to those obtained by Du and Corrales[44] under a similar approach. The calculated cohesive energy (E_c) of monoclinic phase of $Li_2Si_2O_5$ (no. 37) is larger than its corresponding meta-stable phase (no. 60) because it has

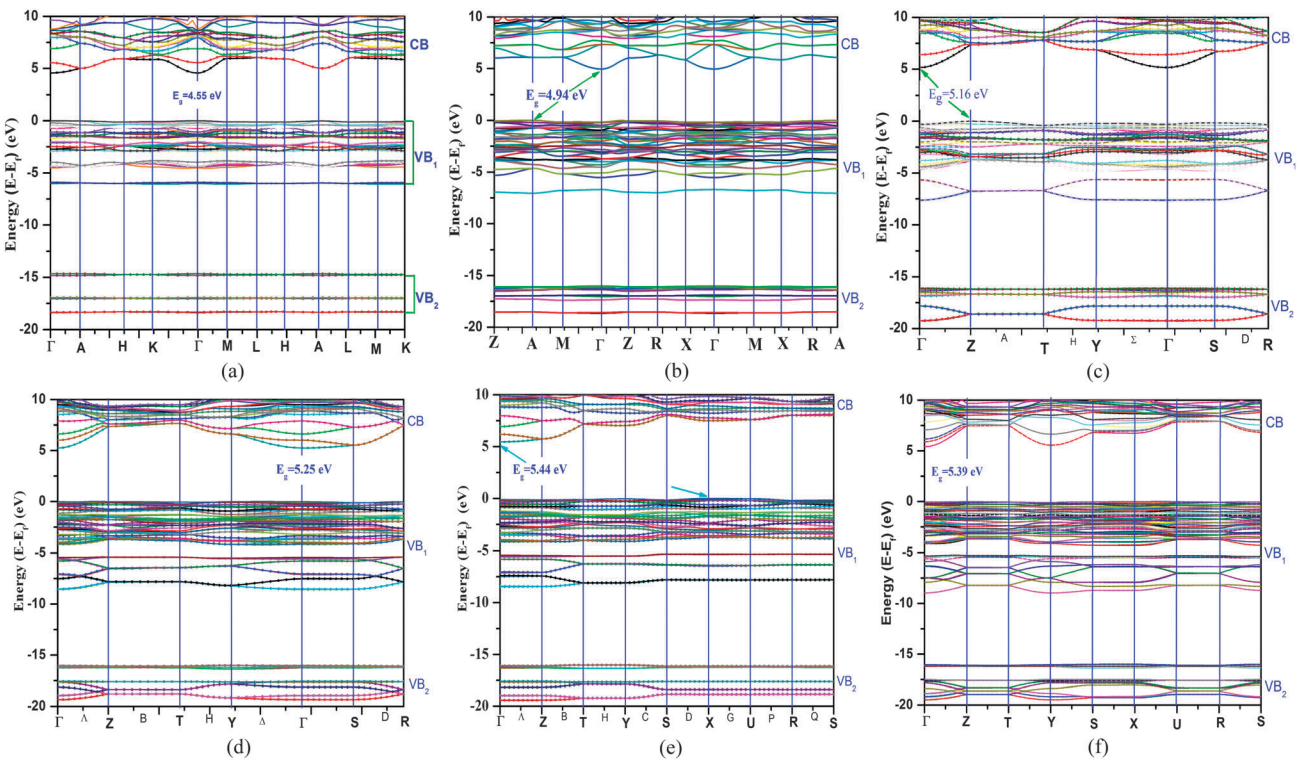

Fig. 3 The calculated band structures of lithium silicates: (a) Li_8SiO_6, (b) $Li_6Si_2O_7$, (c) Li_2SiO_3, (d) $Li_2Si_2O_5$, (e) *meta*-$Li_2Si_2O_5$, (f) $Li_2Si_3O_7$.

slightly lower unit cell energy (E_0) than the meta-stable one as shown in Table 2.

4.2 Electronic properties and band structures

The calculated band structures of various lithium silicates considered in this study are shown in Fig. 3. Within the energy range of −20–10 eV, for all lithium silicates, their valence bands (VBs) can be grouped into two bands: VB_1 and VB_2. Within each VB, there are small gaps to separate them into several sub-bands. The band gaps and bandwidths of these lithium silicates with different Li_2O/SiO_2 ratios are summarized in Table 3.

The calculated total density of states (TDOS) and partial density of states (PDOS) projected onto Li, O, and Si contributions for all of these lithium silicates studied are shown in Fig. 4.

4.2.1 Li_8SiO_6. Among various known lithium silicates, Li_8SiO_6 contains the highest amount of Li_2O component with a Li_2O/SiO_2 ratio of 4 : 1. By comparing the band structure of Li_8SiO_6 indicated in Fig. 3(a) with the band structure of Li_2O reported in ref. 45, it can be seen that similarly to pure Li_2O, Li_8SiO_6 has a direct band gap with a value of 4.55 eV, which is smaller than that of Li_2O (5.39 eV). The first VB is located just below the Fermi level and has a width of 6.19 eV, which is much wider than that of Li_2O. In contrast to Li_2O,[45] the VB_1 of Li_8SiO_6 is separated into four sub-bands by several small gaps as shown in Fig. 3(a). Its second VB is located below −15 eV and was also separated into three narrow sub-bands as listed in Table 3.

From its TDOS and PDOS shown in Fig. 4(a), one can see that in Li_8SiO_6 the p orbitals of Li have a larger contribution than the s orbital and both these components contribute to all VBs and conduction band (CB). The p orbitals of O mainly contribute to VB_1 while its s orbital mainly contributes to VB_2. Both s and p orbitals of Si contribute to the lower portion of VB_1 and VB_2. Obviously, the upper portion of VB_1 is mainly determined by the interactions between Li and O, which are the reacting orbitals to interact with CO_2 during absorption, while the lower portion of VB_1 is determined by interactions among Li, O and Si. Similar to VB_1, the upper sub-band of VB_2 is also mainly determined by the interaction between the s and p orbitals of Li and the s orbital of O, while the lower two sub-bands contain the interactions among the p orbitals of Li, the s orbital of O and the s and p orbitals of Si. From Fig. 2(a), one can see that the Li atoms are just located around the [SiO_4] tetrahedra with various Li–O distances. The shortest Li–O bond is only 1.224 Å. Around each O, there are at most four Li atoms with bond lengths less than 4.0 Å. Since the location of Li atoms is not symmetric with [SiO_4] tetrahedra, the Si–O bond-lengths in the [SiO_4] tetrahedra of Li_8SiO_6 are not equivalent, with the values of 1.449 Å, 1.683 Å, 3.359 Å, and 3.674 Å respectively. The O with the larger Si–O bond length is expected to play a larger role in reactions associated with CO_2 absorption.

4.2.2 $Li_6Si_2O_7$. In $Li_6Si_2O_7$, the Li_2O/SiO_2 ratio is 3 : 2, which is lower than those in Li_8SiO_6 and Li_4SiO_4. Comparing Fig. 3(b) with the band structures of Li_8SiO_6 (Fig. 3(a)) and Li_4SiO_4 reported in ref. 23, one can see that their band structures have similarities, with the VBs separated into several sub-bands by small gaps. However, in contrast to Li_8SiO_6 and Li_4SiO_4, $Li_6Si_2O_7$ has an indirect band gap between the high symmetry points ***A*–*Γ*** with a value of 4.94 eV. Its first VB is located just below the Fermi level and has a width of 7.04 eV, which is much wider than those of Li_2O, Li_8SiO_6 and Li_4SiO_4. As shown in Fig. 3(b) and Table 3, its VB_1 and VB_2 are also separated into two and four sub-bands respectively.

From the TDOS and PDOS as shown in Fig. 4(b), one can see that as in Li_8SiO_6, in $Li_6Si_2O_7$ the p orbitals of Li have larger contributions than its s orbital and all of them involved to form all VBs and CB. The p orbitals of O mainly contribute to VB_1 while its s orbital mainly contributes to VB_2. Both s and p orbitals of Si contribute to the lower portion of VB_1 and VB_2. The upper portion of VB_1 is mainly determined by interactions between Li and O. From Fig. 2(a) and (b) and ref. 23, one can see that in these Li_2O-rich (Li_2O/SiO_2 ratio >1) lithium silicates,

Table 3 The calculated band gaps and the valence band widths of lithium silicates. The corresponding widths of the sub-valence-bands of VB_1 and VB_2 are listed in parentheses. (Unit: eV)

Crystal	VB_2 width	VB_1–VB_2 gap	VB_1 width	Band gap
Li_2O[a]	0.31	12.44	2.59	5.39 (direct)
Li_8SiO_6	3.84 (0.21, 0.21, 0.32)	8.43	6.19 (0.32, 0.64, 0.40, 1.71)	4.55 (direct)
Li_4SiO_4[b]	2.30	9.83	6.17	5.24 (direct)[b]
$Li_6Si_2O_7$	2.77 (0.21, 0.21, 0.11, 0.53)	8.99	7.04 (0.32, 5.44)	4.94 (indirect, ***A*–*Γ***)
Li_2SiO_3	3.15 (1.41, 0.87)	8.47	7.60 (1.95, 4.78)	5.16 (indirect ***Z*–*Γ***) 5.7[d], 7.26[c]
$Li_2Si_2O_5$	3.27 (1.75, 0.33) 2.36[c]	7.53	8.51 (1.09, 1.75, 4.15) 7.51[c]	5.25 (direct) 5.5[d], 7.45[c]
meta-$Li_2Si_2O_5$	3.39 (1.86, 0.33)	7.44	8.54 (1.09, 1.75, 4.27)	5.44 (indirect ***X*–*Γ***) 5.6[d]
$Li_2Si_3O_7$	3.53 (1.99, 0.44)	7.06	8.93 (3.64, 4.30)	5.39 (direct)
α-SiO_2	2.06	7.71	9.44 (4.88, 3.26)	5.75 (indirect, ***F*–*Γ***) 5.84[e], 17.03 (HF)[e]

[a] Ref. 45. [b] Ref. 23. [c] Ref. 38. [d] Ref. 44. [e] Ref. 77.

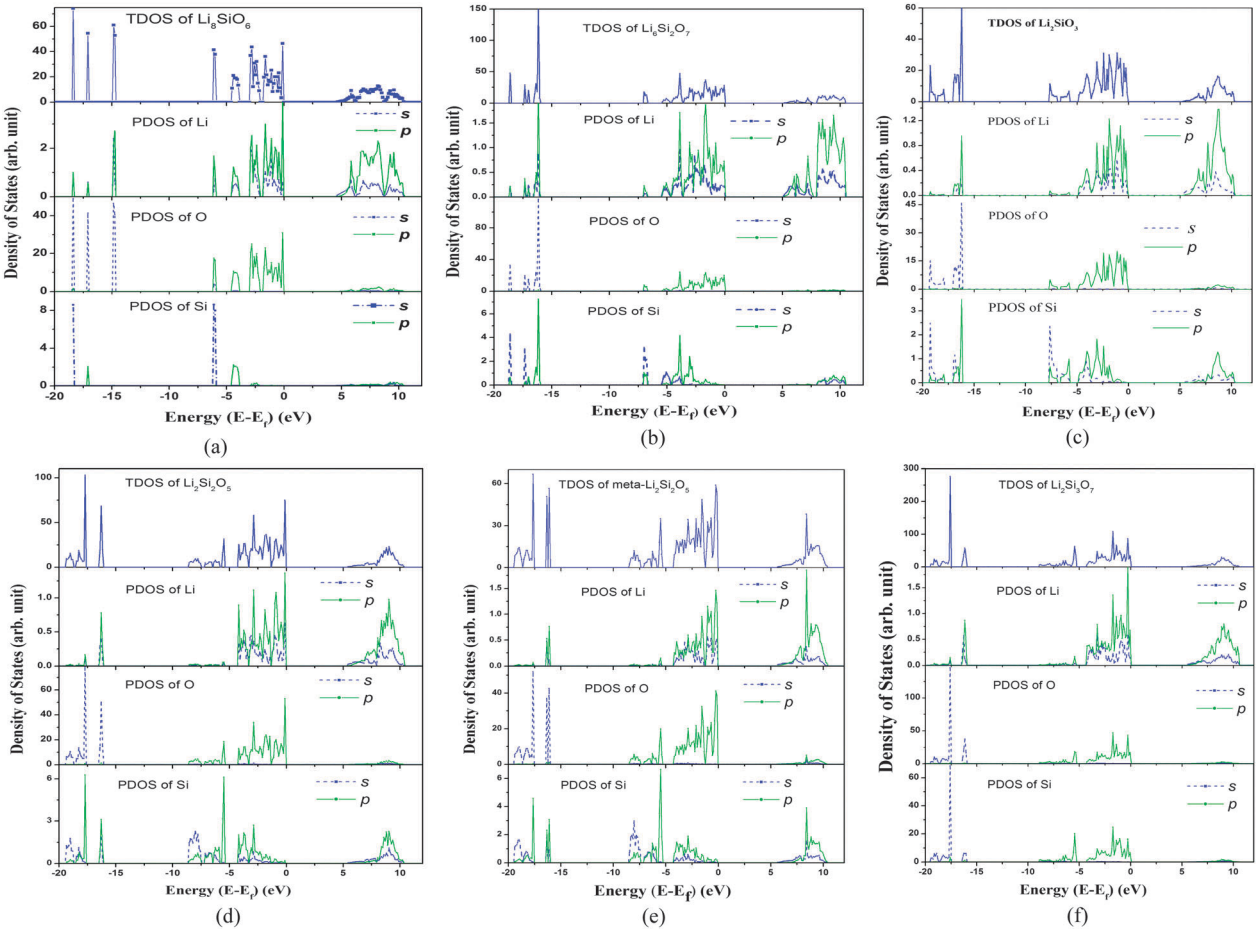

Fig. 4 The calculated density of states of lithium silicates: (a) Li_8SiO_6, (b) $Li_6Si_2O_7$, (c) Li_2SO_3, (d) $Li_2Si_2O_5$, (e) *meta*-$Li_2Si_2O_5$. (f) $Li_2Si_3O_7$.

the [SiO_4] tetrahedra are not bonded to each other and are separated by Li atoms. The Li–O bond-length varies with a shortest length of only 1.931 Å. Since the location of Li atoms is not fully symmetric with [SiO_4], not all the Si–O bond-lengths in [SiO_4] of $Li_6Si_2O_7$ are equal. Unlike Li_8SiO_6, but similar to Li_4SiO_4, the Si–O bond-lengths in $Li_6Si_2O_7$ are much shorter. Two of them are equal with the same value of 1.627 Å and the other two are close with values of 1.640 Å and 1.720 Å, respectively. These findings indicate that the binding between O and Si in $Li_6Si_2O_7$ is stronger than that in Li_8SiO_6.

4.2.3 Li_2SiO_3. Lithium metasilicate, Li_2SiO_3, has a 1 : 1 Li_2O/SiO_2 ratio. As shown in Fig. 3(c), the calculated band gap is an indirect one between the high symmetry points ***Z*** and ***Γ*** of the Brillouin zone with a value of 5.16 eV, which is close to the value of 5.7 eV determined by Du and Corrales[44] using a similar computational method, but lower than the value of 7.26 eV determined by Ching *et al.*[38] using an OLCAO method. Usually, the band-gaps calculated by a Hartree–Fock (HF) method are larger than the experimental measurements. As described in our previous work,[23,24,45,48] due to underestimation of the excited-state energy in standard DFT calculations, our calculated band-gaps are usually smaller than the experimental measurements. Although there is no experimental band gap available for crystalline lithium silicates, it is expected that the real band gap should be between our DFT predictions and the OLCAO values. As shown in Fig. 3(c) and Table 3, within the energy range of −20–0 eV, there are two VBs and each of them is separated into two sub-bands by a small gap. Compared to Li_2O-rich lithium silicates (Li_8SiO_6, Li_4SiO_4, $Li_6Si_2O_7$), the widths of the VBs of Li_2SiO_3 are larger with a reduced gap between VB_1 and VB_2.

From its DOS shown in Fig. 4(c), one can see that in Li_2SiO_3 the upper portion of VB_1 is mainly dominated by s and p orbitals of Li interacting with the p orbitals of O, while the lower portion of VB_1 is mainly dominated by orbitals of Si (sp^3 hybrid) interacting with orbitals of O and Li. Unlike Li_2O-rich lithium silicates, from Fig. 2(c), in Li_2SiO_3, [SiO_4] tetrahedra are bridged to form a chain. Each $[SiO_4]_n$ chain is surrounded by Li atoms. Due to the symmetry, the Si–O bond-lengths in the [SiO_4] tetrahedra of Li_2SiO_3 are divided into two groups with values of 1.61 Å and 1.70 Å respectively.

4.2.4 $Li_2Si_2O_5$. $Li_2Si_2O_5$ has a 1 : 2 Li_2O/SiO_2 ratio and is a SiO_2-rich (Li_2O/SiO_2 ratio <1) lithium silicate. It exists in two phases as shown in Fig. 2(e) and (f). The main difference between them is in the direction in which the silicon oxygen tetrahedra are pointing within the silicon oxygen layers. As shown in Fig. 3(d) and (e), although these two phases have similar band-structure and VB widths, the stable phase (no. 37) has a direct band-gap of 5.25 eV while its meta-stable phase (no. 60)

has an indirect band gap of 5.44 eV between ***X*** and ***Γ*** wave vectors. These values are comparable with the values of 5.5 eV and 5.6 eV respectively calculated by Du and Corrales.[44] However, from their electronic density of states (EDOS) analysis, no information about the band-gap type (direct or indirect) could be obtained. We note that our calculated band gap of the stable Li_2SiO_3 is lower than 7.45 eV obtained by OLCAO.[38] Compared to Li_2SiO_3, these two phases of $Li_2Si_2O_5$ have larger band gaps and wider widths of VB_1 and VB_2.

By comparing Fig. 4(d) and (e), one can see that these two phases have very similar DOS. In both phases, the upper portion of VB_1, which is the most important for reactivity properties (in our case to react with CO_2), is mainly dominated by the interaction of the s and p orbitals of Li and the p orbitals of O. The lower portion of VB_1 is mainly formed by s and p orbitals of Si interacting with the p orbital of O and a small contribution from Li, while their VB_2 are from the interactions among orbitals of Li, O and Si. From Fig. 2(e) and (f), one can see that, similar to Li_2SiO_3, in the two phases of $Li_2Si_2O_5$, the $[SiO_4]$ tetrahedra are bridged to form a chain. Each $[SiO_4]_n$ chain is surrounded with Li atoms. Although the Si–O bond-lengths in $[SiO_4]$ tetrahedra of these two phases are not equal, they are very close to each other. For the stable phase the Si–O bond-lengths are 1.595, 1.628, 1.666, and 1.672 Å while for the meta-stable phase the Si–O bond-lengths are 1.598, 1.626, 1.664, and 1.671 Å respectively.

4.2.5 $Li_2Si_3O_7$. $Li_2Si_3O_7$ is the most SiO_2-rich lithium silicate found in the literature, with a Li_2O/SiO_2 ratio of 1 : 3. As shown in Fig. 3(f), $Li_2Si_3O_7$ has a direct band gap with a value of 5.39 eV. Compared to other SiO_2-rich lithium silicates ($Li_2Si_2O_5$ in Fig. 3(d) and (e)), its VB_1 has a wider band-width and is separated into two sub-bands. Its VB_2 is located below −15 eV and was also separated into two narrow sub-bands.

From its TDOS and PDOS shown in Fig. 4(f), one can see that like other lithium silicates, in $Li_2Si_3O_7$ the p orbitals of Li have a larger contribution than its s orbital and all these orbitals contribute to both VBs and CB. The p orbitals of O mainly contribute to VB_1 while its s orbital mainly contributes to VB_2. Unlike other lithium silicates, in $Li_2Si_3O_7$, the p orbitals of Si have a larger contribution to VB_1 while its s orbital mainly involves in VB_2. As $Li_2Si_3O_7$ is the most SiO_2-rich lithium silicate in this series, the orbitals of Si have a larger influence on VB_1 formation, and therefore, will be significantly involved in interaction with CO_2 during absorption–desorption. From Fig. 2(f), one can see that in $Li_2Si_3O_7$, the $[SiO_4]$ tetrahedra are connected by bridge oxygen and form $[SiO_4]_n$ chain. Li atom layers separate these $[SiO_4]_n$ chains. Again, the Si–O bond-lengths in $[SiO_4]$ of $Li_2Si_3O_7$ are not equal but they have close values of 1.594 Å, 1.631 Å, 1.668 Å, and 1.673 Å respectively.

4.2.6 α-SiO_2. As aforementioned, SiO_2 is used to synthesize these lithium silicates and can also be involved in CO_2 capture reactions. As shown in Table 2, our calculated bulk modulus and cohesive energy of α-SiO_2 are close to experimental data and other theoretical results.[70,71] Fig. 5 shows the calculated band structure and DOS of α-SiO_2. The band gap of α-SiO_2 is indirect between the ***F*** and ***Γ*** high symmetric points with a value of 5.75 eV, in good agreement with other DFT calculated results (5.84 eV).[77] As shown in Fig. 5(a) and Table 3, within the energy range of (−20, 10) eV, the α-SiO_2 also has two VBs with widths of 9.44 eV and 2.06 eV. The gap between these two VBs is 7.71 eV. These two VBs are also separated into two sub-bands with a small gap. From its DOS as shown in Fig. 5(b), the upper portion of VB_1 is mainly the interaction of p orbitals of O and Si while its lower portion is given by contributions of p orbitals of O and s and p orbitals of Si. The VB_2 is mainly from s orbital of O and the s and p orbitals of Si. From Fig. 2(d), one can see that $[SiO_4]$ tetrahedra form a $[SiO_4]_n$ chain structure. Within its unit cell there are three SiO_2 f.u. The calculated results showed that there are three inequivalent $[SiO_4]$ units with different Si–O bond-lengths: (0.980 Å, 1.273 Å, 3.247 Å, 3.384 Å), (1.616 Å, 2.357 Å, 2.831 Å, 3.786 Å), and (2.034 Å, 2.412 Å, 3.201 Å, 3.366 Å).

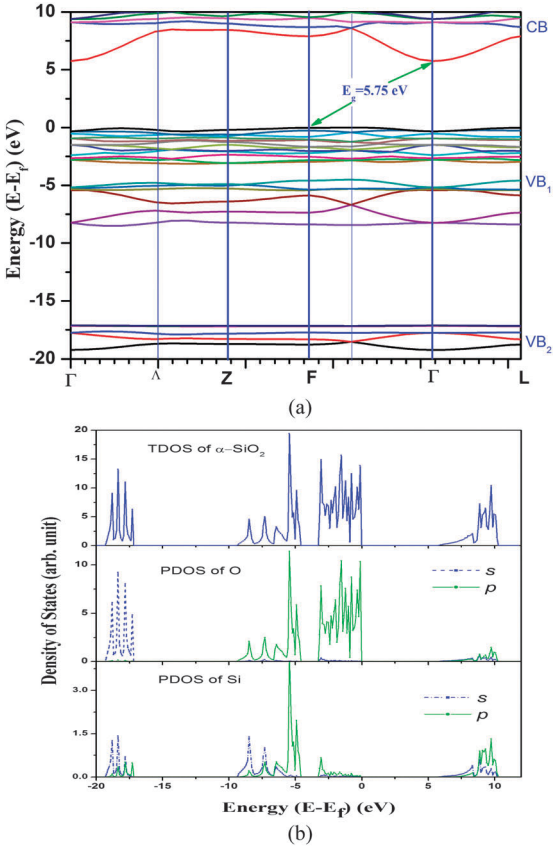

Fig. 5 The calculated electronic properties of α-SiO_2: (a) band structure, (b) density of states.

4.3 Phonon dynamical properties

The calculated phonon dispersions of the set of lithium silicates considered in this study are shown in Fig. 6 while their corresponding total phonon densities of states are shown in Fig. 7.

4.3.1 Li_8SiO_6. As shown in Fig. 2(a) and Table 1, in the Li_8SiO_6 unit cell there are two f.u. Its primitive cell is the same as its unit cell. Therefore, there are 90 phonon modes as shown in Fig. 6(a). Along the ***Γ–A*** wave-vector and around the high symmetry point ***A***, there is a small negligible imaginary frequency

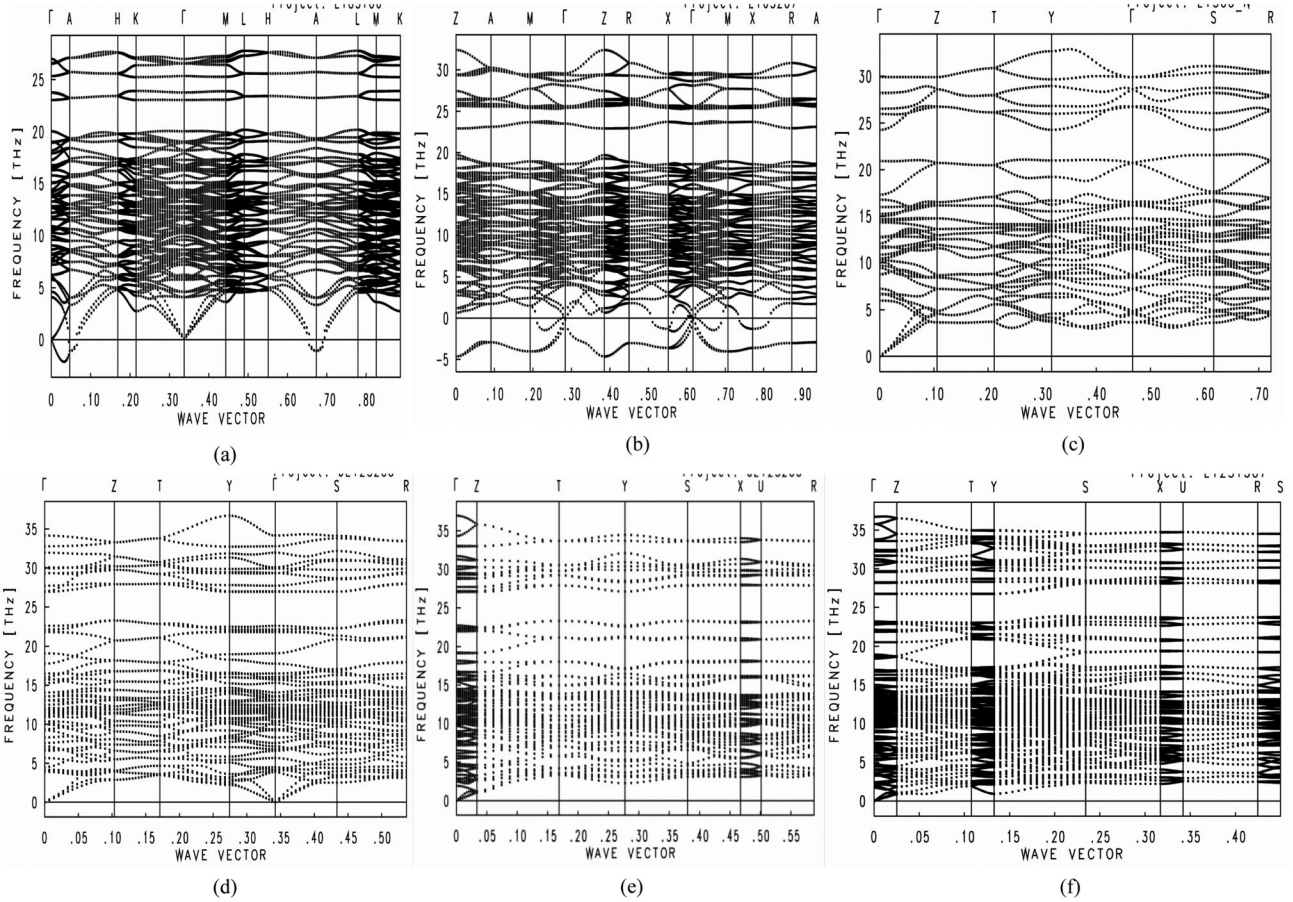

Fig. 6 The calculated phonon dispersions of lithium silicates: (a) Li_8SiO_6, (b) $Li_6Si_2O_7$, (c) Li_2SO_3, (d) $Li_2Si_2O_5$, (e) *meta*-$Li_2Si_2O_5$, and (f) $Li_2Si_3O_7$.

mode (soft mode), indicating instability. Since the space group of Li_8SiO_6 is $P6_3cm$ (no. 185),[60] its corresponding point group is C_{6v}, having the following representation: $10 \otimes (A_1(RI) + B_2) + 5 \otimes (A_2 + B_1) + 15 \otimes (E_1(RI) + E_2(R))$. Obviously, among these vibrational modes, 30 of them ($15 \otimes E_2(R)$) are only Raman (R) active, 40 of them ($10 \otimes A_1(RI) + 15 \otimes E_1(RI)$) are both Infrared (I) and Raman active, while the remaining 20 vibrational modes ($10 \otimes B_2 + 5 \otimes (A_2 + B_1)$) are silent. From its phonon DOS in Fig. 7(a), one can see that along the frequency axis, the amplitude distribution could be grouped into two peaks. The higher frequency (>20 THz) peak is mainly from the Si–O bond vibrations, while the low frequency band (<20 THz) contains contributions from all types of bond vibrations.

4.3.2 $Li_6Si_2O_7$. As shown in Fig. 2(b) and Table 1, in $Li_6Si_2O_7$, both the unit cell and the primitive cell, there are two f.u. Therefore, this system contains 90 phonon modes which are shown in Fig. 6(b). Unlike other lithium silicates, in $Li_6Si_2O_7$ our DFT calculations give two imaginary frequency modes at all wave vectors, indicating that our calculations do not confirm the stability of this reported experimental crystallographic structure. In order to determine what kind of instability is predicted, we explored the dispersion for each inequivalent atom type along *x*-, *y*-, and *z*-directions. Interestingly, as shown in Fig. S1 (in the ESI†), we found that these relaxing modes are only due to motions of O and Si atoms along the *x*- and *y*-directions. These results indicate that along the *xy* plane, the Si–O bonds were constrained and could not be fully relaxed during optimization. Since the space group of $Li_6Si_2O_7$ is $P\bar{4}2_1m$-$D_{2d}{}^3$ (no. 113),[61] its corresponding point group is D_{2d}, having a $23 \otimes E(RI) + 13 \otimes B_2(RI) + 13 \otimes A_1(R) + 9 \otimes B_1(R) + 9 \otimes A_2$ representation. Obviously, among them, 59 vibrational modes ($23 \otimes E(RI) + 13 \otimes B_2(RI)$) are both Infrared and Raman active, 22 vibrational modes ($13 \otimes A_1(R) + 9 \otimes B_1(R)$) are only Raman active, and 9 vibrational modes ($9 \otimes A_2$) are silent. From its phonon DOS in Fig. 7(a), one can see that as a function of frequency, the amplitude of the phonon DOS has three main peaks. One peak appeared below zero frequency (<0 THz), indicating an imaginary frequency or relaxation rather than a vibration, and is due to relaxation of O and Si atoms in the *xy* plane as discussed above (see Fig. 7(a) and Fig. S1, ESI†). From the partial phonon DOS for each type of atom (not shown here), we observed that the high frequency (>20 THz) band contains three peaks and is mainly from contributions of Si and O vibrations, while the low frequency peak (<20 THz) represents all types of bond vibrations. The Li vibration frequencies are mainly between 5 and 15 THz.

4.3.3 Li_2SiO_3. As shown in Fig. 2(d) and Table 1, in the Li_2SiO_3 unit cell there are four f.u. However, its primitive cell only contains two f.u. Therefore, it has 36 phonon modes as shown in Fig. 6(c). Clearly, we predict no instabilities in Li_2SiO_3.

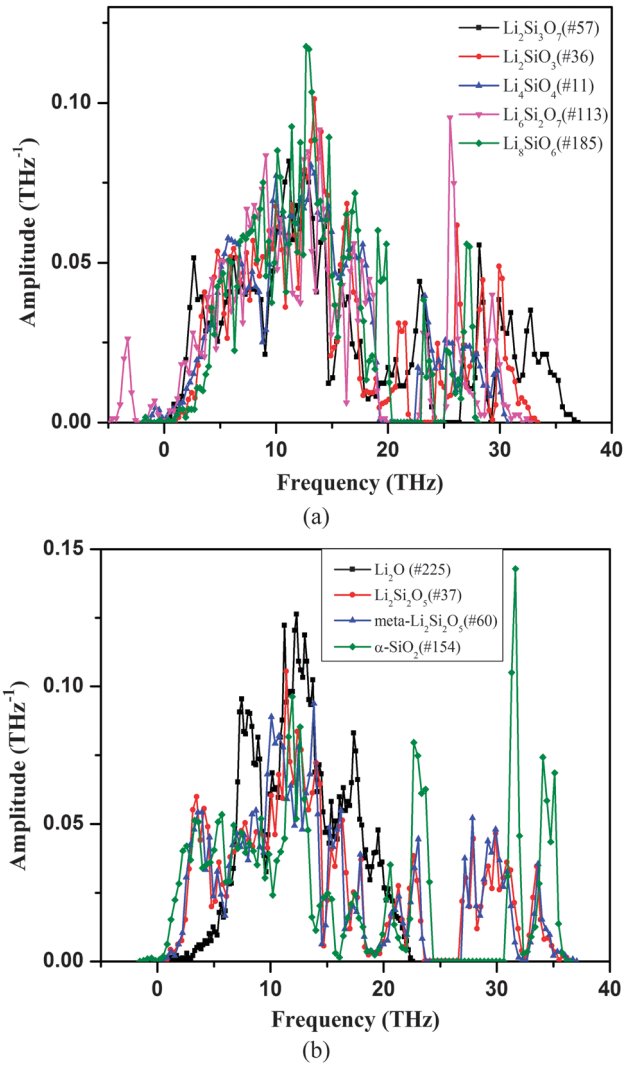

Fig. 7 The calculated phonon total density of states: (a) $Li_2Si_3O_7$, Li_2SiO_3, Li_4SiO_4, $Li_6Si_2O_7$, Li_8SiO_6; (b) Li_2O, α-SiO_2, $Li_2Si_2O_5$, *meta*-$Li_2Si_2O_5$.

Since Li_2SiO_3 is in an orthorhombic structure with space group $Cmc2_1$ (no. 36),[62,63] its corresponding point group is C_{2v}, which represents $10 \otimes (A_1(RI) + B_2(RI)) + 8 \otimes (A_2(R) + B_1(RI))$. Among them, 28 modes are both Raman and Infrared active, and 8 modes are only Raman active. Compared to Li_2O-rich lithium silicates, the vibrational frequencies of Li_2SiO_3 are shifted to higher frequencies. From its phonon DOS in Fig. 7(a) as seen for other Li_2O-rich lithium silicates, the phonon DOS as a function of frequency could be described as having two peaks. The higher frequency (>20 THz) peak is mainly from Si–O bond vibrations, while the low frequency peak (<20 THz) includes contributions from all types of bond vibrations.

4.3.4 $Li_2Si_2O_5$. As shown in Fig. 2(e) and (f) and Table 1, $Li_2Si_2O_5$ has two phases. In its stable phase (no. 37) there are four f.u. in its unit cell, but only two f.u. in its primitive cell, while in its metastable phase (no. 60) there are four f.u. in its both unit cell and primitive cell. Therefore, the metastable phase has twice the number of phonon modes (108 modes) over its stable phase (54 modes), as shown in Fig. 6(d) and (e). Similar to Li_2SiO_3, for this SiO_2-rich lithium silicate, there are no predicted instabilities in either phase. Since the space group of the stable phase of $Li_2Si_2O_5$ is $Ccc2$ (no. 37)[64] and the space group of the meta-stable $Li_2Si_2O_5$ is $Pbcn$ (no. 60),[65] their corresponding point groups are C_{2v} and D_{2h} respectively. Their vibrational frequency modes can be represented by $13 \otimes (A_1(RI) + A_2(R)) + 14 \otimes (B_1(RI) + B_2(RI))$ and $13 \otimes (A_g(R) + A_u + B_{2g}(R) + B_{2u}(I)) + 14 \otimes (B_{1g}(R) + B_{1u}(I) + B_{3g}(R) + B_{3u}(I))$ respectively. In the stable phase, there are 41 vibrational modes both Raman and Infrared active and 13 vibrational modes which are only Raman active. In its metastable phase, there are 54 Raman active vibrational modes, 41 Infrared active modes, and 13 silent modes. From their phonon DOS represented in Fig. 7(b), it can be observed that the frequencies of both phases of $Li_2Si_2O_5$ shift to even higher frequencies related to those of other Li_2O-rich lithium silicates and Li_2SiO_3. Above 27 THz, there are two peaks which are mainly from O and Si vibrations. The Li vibrational frequencies are mainly located between 7 and 17 THz, while the lower peak (<7 THz) is due to contributions from both O and Si vibrations.

4.3.5 $Li_2Si_3O_7$. As shown in Fig. 2(g) and Table 1, the unit cell and the primitive cell of $Li_2Si_3O_7$ coincide and contain four f.u. Therefore, there are 144 phonon modes as shown in Fig. 6(f). There is no unstable relaxation mode predicted for $Li_2Si_3O_7$ when using phonon dispersion calculations. Since the space group of $Li_2Si_3O_7$ is $Pmca$ (no. 57),[37] its corresponding point group is D_{2h}, which has the irreducible representations $19 \otimes (A_g(R) + B_{1g}(R) + B_{2u}(I) + B_{3u}(I)) + 17 \otimes (A_u(I) + B_{1u}(I) + B_{2g}(R) + B_{3g}(R))$. Obviously, among them, 72 vibrational modes are only Raman active, 55 vibrational modes are only Infrared active, and 17 vibrational modes are silent. From its phonon DOS represented in Fig. 7(a), similar to other SiO_2-rich lithium silicates, it was found that the higher frequency (>20 THz) DOS peak is mainly due to Si–O bond vibrations, while the low frequency peak (<20 THz) contains contributions from all types of bond vibrations.

4.3.6 α-SiO_2. As shown in Fig. 2(d) and Table 1, the α-SiO_2 unit cell coincides with its primitive cell and both contain three f.u. Therefore, there are 27 phonon modes in α-SiO_2 as shown in Fig. 8. Along the ***Γ–L*** wave-vector, there is a slow relaxation mode, indicating a slight instability. Since the space group of α-SiO_2 is $P3_221$ (no. 154),[72] its corresponding point group is D_3, which has the irreducible representations $4 \otimes A_1 + 5 \otimes A_2 + 9 \otimes E$ at the

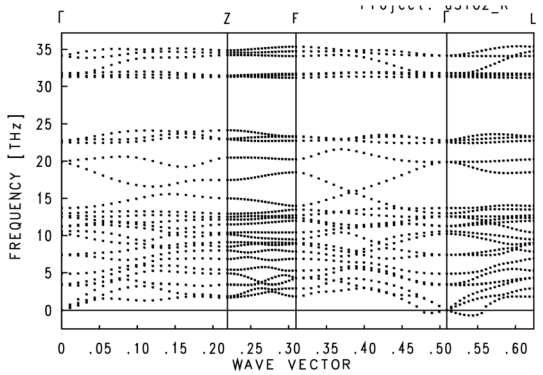

Fig. 8 The calculated phonon dispersions of α-SiO_2.

zone center Γ point.[78] Our calculated frequencies at the Γ point of α-SiO_2 are comparable with other theoretical results[78] and experimental measurements.[79]

Overall, by decreasing the Li_2O/SiO_2 ratio, from Li_8SiO_6 to $Li_6Si_2O_7$, Li_2SiO_3, $Li_2Si_2O_5$, and to $Li_2Si_3O_7$, the frequencies of the vibrational modes are found to increase as shown in Fig. 7.

4.3.7 Phonon free energy and entropy. The calculated phonon free energies and entropies of the above-described lithium silicates and α-SiO_2 *versus* temperature are shown in Fig. 9(a) and (b), respectively. For comparison, the data for Li_4SiO_4[23] and Li_2O[45] are also shown in these figures.

From Fig. 9(a), the zero-point energies (E_{zp}) of these lithium silicates and α-SiO_2 can be obtained and listed in Table 2. Among them, Li_8SiO_6, $Li_6Si_2O_7$ and $Li_2Si_3O_7$ have larger E_{zp} values. However, with increasing temperature, their phonon free energies decrease faster. These results indicate that in different temperature regions, their thermodynamic properties could be different. The E_{zp} of these lithium silicates make significant contributions to the prediction of thermodynamic properties as indicated in eqn (2).

The entropies of these lithium silicates and α-SiO_2 at 300 K are listed in Table 2. From Fig. 9(b), one can see that, at 0 K, the entropies are zero and increase with increasing temperature. Additionally, we note that the calculated entropy of Li_2SiO_3 (83.18 J mol^{-1} K at 300 K) is very close to the experimental value (81.97 J mol^{-1} K at 300 K) from HSC Chemistry Database,[76] which indicates that our theoretical approach can predict sufficiently accurate the experimentally measured thermodynamic properties of these solids.

By comparing the data for both phases of $Li_2Si_2O_5$, we can see that although these two phases of $Li_2Si_2O_5$ have different electronic and phonon dispersion features, their thermodynamic data are very close to each other. Therefore, in the following thermodynamic analysis, we only use the thermodynamic properties of the stable phase.

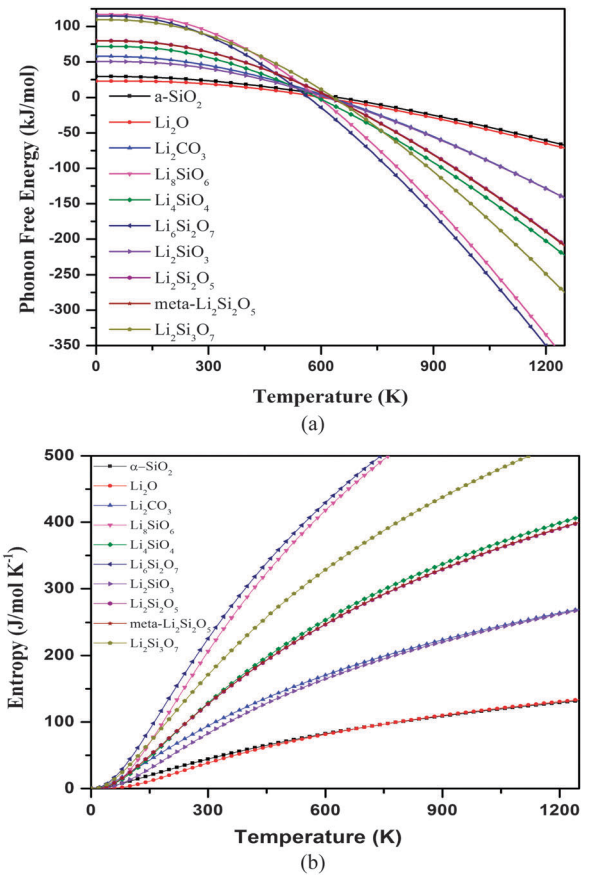

Fig. 9 (a) The calculated phonon free energies of lithium silicates in which the zero point energy included; (b) the calculated entropies of lithium silicates and Li_2O and α-SiO_2.

4.4 Structural transformation

By changing the SiO_2/Li_2O ratio, several phase transformations among these lithium silicates can happen as indicated in Table 4. The corresponding calculated energy change (ΔE^{DFT}) and the thermodynamic properties (ΔH, ΔG) for each reaction are also listed in Table 4.

From the phase diagram shown in Fig. 1, the reactions (1)–(6) show that the corresponding lithium silicate phases can be transformed to the closest phase with lower Li_2O/SiO_2 ratio by adding more SiO_2. As the ΔH and ΔG of these reactions (1)–(6) are negative, thermodynamically, these phase transformations can take place spontaneously once the SiO_2 is available. Since $Li_2Si_3O_7$ has the highest SiO_2 content in this series and in the literature no evidence showed even higher SiO_2 content silicate available, here, we consider that $Li_2Si_3O_7$ does not react with SiO_2 to form even high SiO_2 content silicate.

As shown in Table 4, reactions (2a)–(7a) indicate that the lithium silicate phases can be intermediates to the adjacent two phases as shown in Fig. 1. However, only $Li_6Si_2O_7$ in reaction (4a) could be transformed to its adjacent phases (Li_4SiO_4 and Li_2SiO_3) at ambient conditions as its ΔH and ΔG are less than zero. Li_8SiO_6 in reaction (2a) could be transformed to Li_4SiO_4 and Li_2O by supplying some energy as its ΔH and ΔG have small positive values. By adding energy (*e.g.* by increasing temperature), this reaction could go forward. As for reaction (3a), its free energy is also positive (25.17 kJ mol^{-1}), to convert Li_4SiO_4 into Li_8SiO_6 and $Li_6Si_2O_7$ also needs input energy. Obviously, among these Li_2O-rich lithium silicates, Li_4SiO_4 is the most stable phase. As shown by reaction (5a) in Table 4, it is possible to convert Li_2SiO_3 into its adjacent silicates ($Li_6Si_2O_7$ and $Li_2Si_2O_5$) by adding extra energy as its ΔH and ΔG have small positive values. Similarly, for those SiO_2-rich lithium silicates ($Li_2Si_2O_5$ and $Li_2Si_3O_7$), reactions (6a) and (7a) may be driven forward by providing extra energy.

Reactions (3b), (5b), (6b), and (7b) reveal that under normal conditions these lithium silicates (Li_4SiO_4, Li_2SiO_3, $Li_2Si_2O_5$, and $Li_2Si_3O_7$) cannot release Li_2O to form low Li_2O/SiO_2 ratio lithium silicates. Instead, as shown in Table 4 the reverse reactions can occur at ambient conditions. In other words, by adding Li_2O into low Li_2O/SiO_2 ratio lithium silicates, we can obtain new lithium silicate phases with higher Li_2O/SiO_2 ratios.

4.5 Capabilities of lithium silicates for CO_2 capture

As described in the first section, among the lithium silicates considered in this study, Li_4SiO_4 was widely investigated as

Table 4 The phase transition reactions among various lithium silicates and the corresponding calculated energy changes (ΔE^{DFT}), heat of reaction (ΔH), and Gibbs free energy change (ΔG) at T = 300 K (unit: kJ mol^{-1})

Reactions	ΔE^{DFT}	ΔH	ΔG
$Li_2O + \frac{1}{4}SiO_2 \leftrightarrow \frac{1}{4}Li_8SiO_6$ (1)	−50.2	−50.8	−51.4
$Li_8SiO_6 + SiO_2 \leftrightarrow 2Li_4SiO_4$ (2)	−174.3	−176.4	−178.4
$Li_8SiO_6 \leftrightarrow Li_4SiO_4 + 2Li_2O$ (2a)	13.2	13.30	13.56
$Li_4SiO_4 + \frac{1}{3}SiO_2 \leftrightarrow \frac{2}{3}Li_6Si_2O_7$ (3)	−11.3	−15.4	−17.5
$Li_4SiO_4 \leftrightarrow \frac{1}{5}Li_8SiO_6 + \frac{1}{5}Li_6Si_2O_7$ (3a)	28.1	26.03	25.2
$Li_4SiO_4 \leftrightarrow Li_2SiO_3 + Li_2O$ (3b)	56.4	57.3	59.4
		82.7[a]	83.7[a]
$Li_6Si_2O_7 + SiO_2 \leftrightarrow 3Li_2SiO_3$ (4)	−95.2	−89.7	−83.6
$Li_6Si_2O_7 \leftrightarrow Li_4SiO_4 + Li_2SiO_3$ (4a)	−20.5	−14.5	−10.3
$Li_2SiO_3 + SiO_2 \leftrightarrow Li_2Si_2O_5$ (5)	−7.3	−7.1	−6.9
		0.6[a]	1.7[a]
$Li_2SiO_3 \leftrightarrow \frac{1}{4}Li_6Si_2O_7 + \frac{1}{4}Li_2Si_2O_5$ (5a)	22.0	20.6	19.2
$Li_2SiO_3 \leftrightarrow Li_2O + SiO_2$ (5b)	131.2	132.5	132.6
		140.8[a]	141.1[a]
$Li_2Si_2O_5 + SiO_2 \leftrightarrow Li_2Si_3O_7$ (6)	−2.9	−2.7	−2.6
$Li_2Si_2O_5 \leftrightarrow \frac{1}{4}Li_2SiO_3 + \frac{1}{2}Li_2Si_3O_7$ (6a)	2.2	2.2	2.2
$Li_2Si_2O_5 \leftrightarrow Li_2O + 2SiO_2$ (6b)	138.4	139.6	139.6
		141.3[a]	142.9[a]
$Li_2Si_3O_7 \leftrightarrow Li_2Si_2O_5 + SiO_2$ (7a)	2.9	2.7	2.6
$Li_2Si_3O_7 \leftrightarrow Li_2O + 3SiO_2$ (7b)	141.3	142.3	142.2

[a] Calculated from HSC Chemistry package[76] at T = 303.15 K. The Li_4SiO_4, Li_2SiO_3 and $Li_2Si_2O_5$ in this database are the mixtures $2Li_2O{\cdot}SiO_2$, $Li_2O{\cdot}SiO_2$ and $Li_2O{\cdot}2SiO_2$ respectively.

a high-temperature CO_2 sorbent using both experimental measurements[1,7,14,15,17,21,26,28,29,80] and theoretical methods.[23] For Li_2SiO_3, Khomane *et al.*[81] found that this can absorb CO_2 up to 610 °C and release CO_2 above 630 °C. Venegas *et al.*[17] found that Li_4SiO_4 first captured CO_2 to form Li_2CO_3 and Li_2SiO_3, then, some of the Li_2SiO_3 further reacted with CO_2 to form SiO_2 and Li_2CO_3. It was also found that the kinetic behavior of CO_2 absorption on Li_2SiO_3 is much slower than that on Li_4SiO_4.[16] Recently, Durán-Muñoz *et al.*[32] explored the CO_2 capture properties of Li_8SiO_6 and found that Li_8SiO_6 can absorb CO_2 over a wide temperature range with a maximum capacity of 11.8 mmol CO_2 per gram Li_8SiO_6. Their results also showed that the CO_2 capture mechanism of Li_8SiO_6 is temperature dependent. Apart from these three lithium silicates (Li_8SiO_6, Li_4SiO_4, Li_2SiO_3), no other reports on CO_2 capture by other lithium silicates could be found.

4.5.1 Thermodynamic properties of lithium silicates capturing CO_2. We used the calculated thermodynamic properties of the Li_2O–SiO_2 series of lithium silicates reported above, together with the calculated thermodynamic properties of Li_2CO_3 which we previously reported[45] in order to compute the temperature dependence of the free energy differences described by eqn (2) and (3). This analysis has been done for the series of CO_2 capture reactions indicated in Fig. 10 and in Table 5. Specifically, we used the heat of reactions (enthalpy change ΔH) and Gibbs free energy differences (ΔG, in this case same as $\Delta\mu^0$) associated with the solid component alone, for which we ignore any pressure dependence. For those lithium silicates (Li_8SiO_6, Li_4SiO_4, $Li_6Si_2O_7$) with the Li_2O/SiO_2 ratio greater than one, we also considered their CO_2 capture reactions with two steps: first to form Li_2SiO_3, then to form SiO_2.

It is generally accepted that the CO_2 capacity of solid sorbents should be above 3 mol CO_2 per kilogram solid (~15 wt%) in order to meet the industrial requirements and have a chance of providing energy reductions of 30–50% or more compared to the optimum aqueous-MEA-based process.[82] As shown in Table 5, the theoretical CO_2 weight percentage maxima of all these lithium silicates are greater than this minimum requirement (>15 wt%). Therefore, from the CO_2 capture capacity point of view, all of these systems could meet this criterion to be used as CO_2 sorbents.

From Fig. 10 and Table 5, one can see that when going from Li_2O to $Li_2Si_3O_7$ by decreasing the Li_2O/SiO_2 ratio, the calculated ΔH and ΔG values of the corresponding CO_2 capture reactions are decreased (less negative). Throughout the entire temperature range as shown in Fig. 10(a), only three CO_2 capture reactions by $Li_2Si_3O_7$, $Li_2Si_2O_5$ and Li_2SiO_3 have ΔH greater than zero starting at 640 K, 840 K, and 1320 K, respectively. Since $\Delta G = \Delta H - T\Delta S$, as shown in Fig. 10(b) the Gibbs free energies of these reactions can be positive starting from a certain temperature for each reaction. In this subsection we call the temperature at which ΔG changes its sign as the turnover temperature. From Fig. 10(b) one can see that these reactions could be grouped into four categories: $Li_2Si_3O_7$, $Li_2Si_2O_5$ and Li_2SiO_3 systems, with a Li_2O/SiO_2 ratio ≥1.0, have the lowest turnover temperatures (365 K, 345 K, 425 K respectively); Li_2O and Li_8SiO_6 (Li_2O/SiO_2 = 4 : 1, partially transform to Li_2SiO_3) have the highest turnover temperatures (1155 K and 1105 K), while Li_4SiO_4 and $Li_6Si_2O_7$ have medium turnover temperatures (600–900 K). Among them, Li_4SiO_4 has the lowest turnover temperature and forms a single group, while $Li_6Si_2O_7$ and Li_8SiO_6 formed another group with higher turnover temperatures.

4.5.2 The relationship among the chemical potential, temperature, and the CO_2 pressure. According to eqn (1) and (4), we can explore the relationship among the chemical potential ($\Delta\mu(T,P)$), the temperature, and the CO_2 pressure (P_{CO_2}) of the set of CO_2 capture reactions by various lithium silicates.

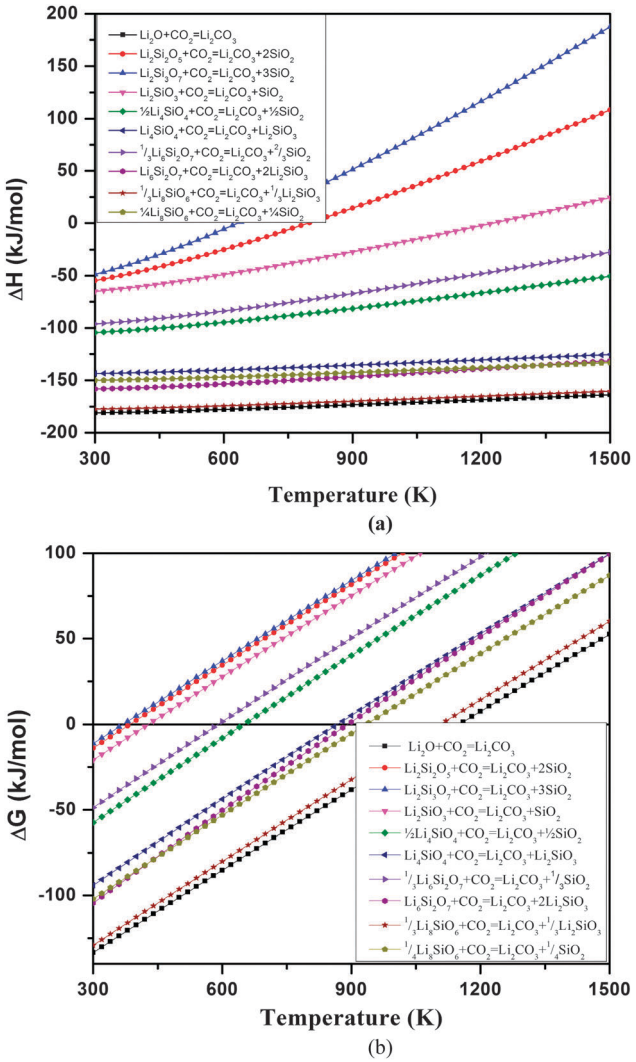

Fig. 10 The calculated thermodynamic properties of the reactions for lithium silicates capture CO_2 *versus* temperature: (a) heat of reaction *versus* temperature; (b) Gibbs free energy *versus* temperature.

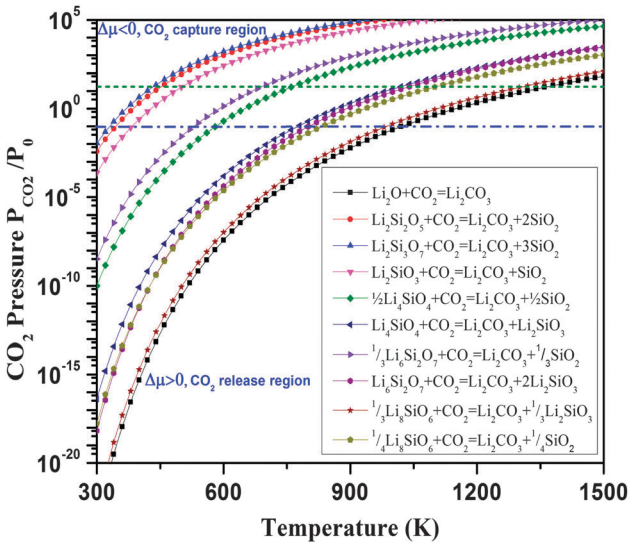

Fig. 11 Contour plots of the calculated chemical potential ($\Delta\mu$) *versus* temperature and the CO_2 pressure (P plotted on the logarithmic scale) for the CO_2 capture reactions. Only the $\Delta\mu = 0$ curve is shown explicitly. For each reaction, above its $\Delta\mu = 0$ curve, their $\Delta\mu < 0$, which means the sorbents absorb CO_2 and the reaction goes forward, whereas below the $\Delta\mu = 0$ curve, their $\Delta\mu > 0$, which indicates CO_2 starts to be released and reaction goes backward with regeneration of the sorbents.

These corresponding results are shown in Fig. 11. The lines in this figure give the values of T and P for which $\Delta\mu(T,P) = 0$ for each reaction. Around each line is a good region for absorption and desorption with optimal conditions because of the minimal energy costs at the respective temperature and pressure conditions. Above the lines, the respective reactions are driven in the CO_2 absorption direction and Li_2CO_3 is formed, while below the respective lines the reactions are driven in the opposite direction, releasing CO_2 and regenerating the lithium silicate solid.

As aforementioned and shown in Fig. 11, all of the reactions are thermodynamically favorable over a certain range of temperatures and P_{CO_2}, which means that under such conditions CO_2 is thermodynamically favored to be captured by these lithium silicates. Obviously, with increasing Li_2O/SiO_2 ratio, the CO_2 absorption by these lithium silicates becomes more exothermic and a large amount of heat is released as shown in Fig. 10(a). Such heat will drive the system to higher temperature where absorption might be stopped. Therefore, the heat resulting from the reaction must be removed from the system and re-used in order to reduce the overall costs.

Table 5 The maximum weight percentages of CO_2 capture capacity of lithium silicates, the calculated thermodynamic properties of reactions of CO_2 captured by these lithium silicates at $T = 300$ K (in kJ mol^{-1}); highest temperature for lithium silicates capturing CO_2 at pre-combustion (T_1) ($P_{CO_2} = 20$ bar) and post-combustion (T_2) ($P_{CO_2} = 0.1$ bar) conditions are also listed

Reaction	Wt%	ΔE_{DFT}	ΔE_{ZP}	ΔH	ΔG	T_1	T_2
$Li_2O + CO_2 \leftrightarrow Li_2CO_3$	147.28	−203.96	4.52	−180.89	−133.42	1375	1025
$\frac{1}{3}Li_8SiO_6 + CO_2 \leftrightarrow Li_2CO_3 + \frac{1}{3}Li_2SiO_3$	73.51	−181.97	5.16	−177.37	−129.11	1325	985
$\frac{1}{4}Li_8SiO_6 + CO_2 \leftrightarrow Li_2CO_3 + \frac{1}{4}SiO_2$	98.01	−154.99	5.42	−150.13	−102.04	1115	835
$Li_4SiO_4 + CO_2 \leftrightarrow Li_2CO_3 + Li_2SiO_3$	36.72	−148.78	5.97	−143.55	−94.05	1025	775
$\frac{1}{2}Li_4SiO_4 + CO_2 \leftrightarrow Li_2CO_3 + \frac{1}{2}SiO_2$	73.44	−111.42	6.07	−104.36	−57.44	765	585
$Li_6Si_2O_7 + CO_2 \leftrightarrow Li_2CO_3 + 2Li_2SiO_3$	20.98	−169.26	13.09	−158.09	−104.38	1045	805
$\frac{1}{3}Li_6Si_2O_7 + CO_2 \leftrightarrow Li_2CO_3 + \frac{2}{3}SiO_2$	62.93	−105.79	8.48	−96.08	−48.68	695	525
$Li_2SiO_3 + CO_2 \leftrightarrow Li_2CO_3 + SiO_2$	48.92	−74.06	6.18	−65.08	−20.83	505	385
$Li_2Si_2O_5 + CO_2 \leftrightarrow Li_2CO_3 + 2SiO_2$	29.33	−66.75	5.90	−54.06	−13.87	455	345
$Li_2Si_3O_7 + CO_2 \leftrightarrow Li_2CO_3 + 3SiO_2$	20.94	−63.83	5.52	−48.60	−11.26	435	335

The operating conditions for absorption–desorption processes depend on the specific pre- and post-combustion technologies. Under pre-combustion conditions, after water-gas shift, the gas stream mainly contains CO_2, H_2O and H_2. The partial CO_2 pressure is around 15–25 bar and the temperature is around 523–773 K. To minimize the energy consumption, the ideal sorbents should work in these pressure and temperature ranges to separate CO_2 from H_2. We define T_1 for each reaction to be the temperature at which the $\Delta\mu(P,T) = 0$ curve crosses the $P = 20$ bar line in Fig. 11. This temperature T_1, listed in Table 5, is the temperature above which the lithium silicate cannot absorb CO_2 anymore and will start to release CO_2 when the CO_2 partial pressure is 20 bar. This indicates that, during capture of CO_2, the operating temperature should be lower than T_1, whereas the operating temperature must be higher than T_1 in order to release CO_2. For post-combustion conditions, the gas stream mainly contains CO_2 and N_2, the partial pressure of CO_2 is around 0.1–0.2 bar, and the temperature range is quite different. We similarly define T_2 to be the temperature at which the $\Delta\mu = 0$ curve for each reaction crosses the horizontal $P = 0.1$ bar line in Fig. 11. These corresponding T_2 values obtained for post-combustion capture by these lithium silicates are also listed in Table 5.

Obviously, the T_1 and T_2 values listed in Table 5 are the highest temperatures at which the CO_2 absorption reaction still can occur for the specific pre- and respectively post-combustion conditions. However, depending on which capture technology is considered, the real capture temperatures should be lower than what we showed in Table 5 (T_1 and T_2). The United States Department of Energy (US-DOE) programmatic goal for post-combustion CO_2 capture is to capture at least 90% CO_2 with an increase in the cost of electricity of no more than 35%, whereas in the case of pre-combustion CO_2 capture it is to capture at least 90% CO_2 with an increase in the cost of electricity of no more than 10%.[83] Assuming that 90% of the CO_2 is captured, the final CO_2 partial pressure will be lower than its initial value at 0.01–0.02 bar for post-combustion and at 1.5–2.5 bar for pre-combustion. Therefore, at the end, the final T_1 and T_2 shift to a lower temperature range. Generally speaking, at high temperature the kinetics is faster. From the kinetics point of view, the capture temperature should be as close to the corresponding T_1 and T_2 as possible. However, as aforementioned the capture process is exothermic; during CO_2 capture, the system temperature will be increased even when heat-exchangers are used. Therefore, the practical operating temperature should be lower than T_1 and T_2 for pre- and post-combustion technologies respectively.

However, as a CO_2 solid sorbent, the materials of interest should not only be able to absorb CO_2 easily, but also easily release the CO_2 from the products. As shown in Fig. 10 and 11, to reverse the CO_2 capture reaction (a), energy input is needed as these reverse reactions are endothermic. Obviously, the operating temperature for CO_2 desorption should be higher than the indicated temperatures T_1 (pre-combustion) or T_2 (post-combustion) as shown in Fig. 11.

From Fig. 10 and 11, one can see that during absorption of CO_2, the lithium silicates with Li_2O/SiO_2 ratio >1 (*e.g.* Li_8SiO_6, $Li_6Si_2O_7$, Li_4SiO_4) can be fully converted into SiO_2 and Li_2CO_3 because thermodynamically Li_2SiO_3 can further absorb CO_2 to gain energetic advantage. As shown in Fig. 11, for these Li_2O-rich lithium silicates, in order to obtain maximum CO_2 capture capacity, the operating temperatures during capture should be lower than the turnover temperatures (T_1 for pre-combustion capture or T_2 for post-combustion capture) of Li_2SiO_3. If the capture temperature is higher than that temperature for Li_2SiO_3, the reverse reaction ($Li_2CO_3 + SiO_2 = Li_2SiO_3 + CO_2$) will start and the products will be Li_2SiO_3 and Li_2CO_3. In this case, the CO_2 capture capacities of these Li_2O-rich lithium silicates could not reach their maxima. However, during regeneration, when Li_2CO_3 and Li_2SiO_3 (or SiO_2) react with each other to release CO_2 and regenerate the sorbent, the temperature is the key factor to ensure that the original lithium silicate is being regenerated. Actually, from Fig. 11 one can see that from the "CO_2 capture region" to the "CO_2 release region" we can have different regenerating temperatures for different silicates. For example, even if one uses Li_8SiO_6 to capture CO_2, if the regenerating temperature is lower than its corresponding T_1 or T_2 in Table 5, one cannot obtain Li_8SiO_6, but instead other silicates with lower Li_2O/SiO_2 ratios will be formed. Durán-Muñoz *et al.*[32] measured the XRD pattern of Li_8SiO_6 capture CO_2 at 550 °C and 650 °C and found that the products contain Li_4SiO_4 and Li_2SiO_3, which reflect the fact that Li_8SiO_6 first absorbs $2CO_2$ to form Li_2CO_3 and Li_4SiO_4, then Li_4SiO_4 further absorbs another CO_2 to form Li_2CO_3 and Li_2SiO_3. Similar results were obtained by Qi *et al.*[84] Their results showed that in a temperature range of 25–228 °C, Li_4SiO_4 could fully react with CO_2 to form Li_2CO_3 and SiO_2 with highest CO_2 capacity as shown in Table 5. In the temperature range of 229–262 °C, Li_4SiO_4 absorbs CO_2 to form Li_2CO_3 and $Li_2Si_2O_5$, and above 262 °C, the Li_4SiO_4 absorbs CO_2 only to form Li_2SiO_3 and Li_2CO_3 with lower CO_2 capture capacity. Such experimental evidence is in good agreement with our theoretical predictions. Although in the literature, there is no experimental study on CO_2 captured by $Li_6Si_2O_7$, from our calculated results in Fig. 11, it can be seen that its CO_2 capture behavior should be intermediate between Li_4SiO_4 and Li_2SiO_3.

Among these lithium silicates, we present experimental results on Li_8SiO_6, Li_4SiO_4 and Li_2SiO_3 as possible CO_2 captors.[16,32,85,86] Here, Fig. 12 shows our dynamic TGA data on the CO_2 capture of these lithium silicates, in addition to the Li_2O. From these curves, it is clearly seen how the Li_2O/SiO_2 ratio modified the amount of CO_2 captured and the temperature range in which the process is performed. We note that these experiments are not quantitative, thus the weight increase analysis must be performed in other types of experiments presented below. From the temperature point of view, it is evident that all the silicates captured CO_2 in two different steps, as it was previously described. Analyzing the Li_2O, as example, the first CO_2 capture process occurred between 180 and 380 °C. The weight increase at this stage is associated with the CO_2 superficial reaction. Then, once the diffusion processes are activated, the second weight increment was produced between 580 and 710 °C. Here, the CO_2 capture is produced in the silicate bulk. A similar interpretation is possible for the other curves depicted as an

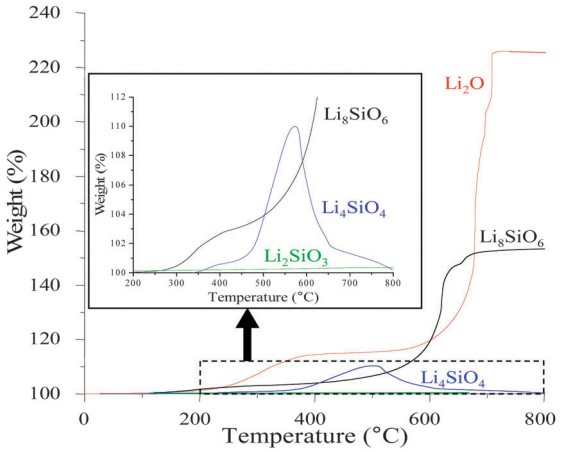

Fig. 12 Dynamic thermogravimetric analyses of different lithium silicates (Li_2O, Li_8SiO_6, Li_4SiO_4 and Li_2SiO_3) into a CO_2 flux (60 mL min^{-1}).

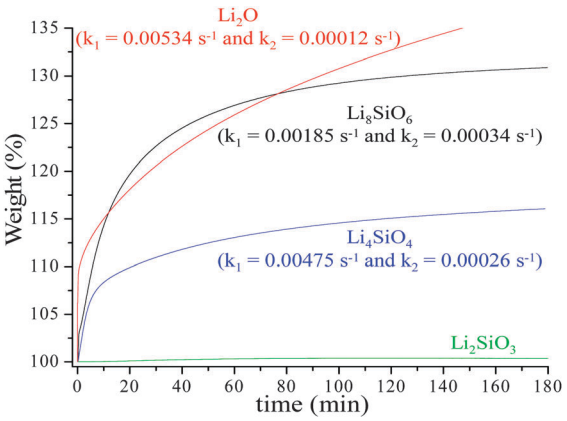

Fig. 13 CO_2 isothermal experiments performed at 600 °C in the following lithium silicates: Li_8SiO_6, Li_4SiO_4, Li_2SiO_3 and Li_2O. The *k* constant values reported correspond to the isothermal fitting to a double exponential model.

inset in Fig. 12, although the reaction process and the external shell composition may differ in each lithium silicate whose reactions are proposed in Table 5.

The maximum temperature, at which each lithium silicate is able to trap CO_2, has the following trend: Li_2O > Li_8SiO_6 > Li_4SiO_4 > Li_2SiO_3, at which the CO_2 capture properties of Li_2SiO_3 can be considered as negligible. These results are in good agreement with our theoretical results presented in Fig. 11 and in Table 5. Therefore, based on these results, if the non-tested lithium silicates were evaluated as possible CO_2 capture sorbent, the $Li_6Si_2O_7$ (Li_2O/SiO_2 ratio higher than that of Li_2SiO_3) could present some interesting properties.

Except for those Li_2O-rich lithium silicates, our calculated results also showed that thermodynamically SiO_2-rich lithium silicates (Li_2SiO_3, $Li_2Si_2O_5$, and $Li_2Si_3O_7$) could absorb CO_2 at even lower temperatures. However, the experimental data showed that the Li_2SiO_3 had a very small CO_2 capture capacity. We suggest that this disagreement between prediction and experiment arises because the capture reaction rates of the SiO_2-rich lithium silicates are very slow. To consider this possibility further we discuss the kinetics of CO_2 capture by lithium silicates in the following section.

4.5.3 The kinetics of lithium silicates capturing CO_2. Kinetically, it is generally accepted that the CO_2 capture of lithium silicates is a two-step process. Initially, the lithium silicate particles react with CO_2 at the particle surface. This superficial reaction involves the formation of an external shell composed of lithium carbonate and a metal oxide or a lithium secondary phase, depending on the initial composition.[87] Once the first stage is complete, bulk diffusion processes must be activated for the silicate to continue CO_2 chemisorption.[87,88]

As discussed in previous section, depending on the operating temperature, the Li_2O-rich lithium silicates capturing CO_2 can lead to different products. Our experimental results showed that Li_2O only produces Li_2CO_3, but Li_8SiO_6, Li_4SiO_4 and Li_2SiO_3 produce more complex external shell compositions. Li_8SiO_6 produces two consecutive reactions: (1) $Li_8SiO_6 + 2CO_2 = Li_4SiO_4 + 2Li_2CO_3$ and (2) $Li_4SiO_4 + CO_2 = Li_2SiO_3 + Li_2CO_3$. In fact, the second consecutive CO_2 capture process is evident in the corresponding dynamic TGA experiment (Li_8SiO_6) between 630 and 670 °C. Li_4SiO_4 presents the second reaction proposed just above the Li_8SiO_6 curve while Li_2SiO_3 hardly reacts at all.

It must be mentioned that there is not general agreement about the second weight increase (CO_2 capture controlled by the diffusion processes). While some authors proposed CO_2 diffusion, others proposed Li^+ and O^{2-} ionic diffusion. In any case, the whole diffusion process is highly controlled by the chemical composition and the microstructure of the external shell, which is composed of a mixture of Li_2CO_3 and/or lithium secondary phases and/or metal oxides.[87,88]

Fig. 13 shows the CO_2 isothermal weight gain due to CO_2 absorption as a function of time of the same lithium silicates (Li_2O, Li_8SiO_6, Li_4SiO_4 and Li_2SiO_3), at 600 °C. Qualitatively, at short times (~10 min) the CO_2 capture rates for the lithium silicates are ordered as follows (fastest first): Li_2O > Li_8SiO_6 > Li_4SiO_4 > Li_2SiO_3, and the same trend is observed for long times (~80 min). The only significant variation of this tendency was observed between Li_2O and Li_8SiO_6 in the 10 to 80 min interval. At t < 10 min, the curves' behaviors were inverted and Li_8SiO_6 started to absorb faster than Li_2O up to 80 min. This effect can be attributed to the diffusion process that must control the reaction process. Therefore, different microstructural features may have induced this change. At t > 80 min, Li_2O captures more CO_2 than Li_8SiO_6 due to chemical capacity of both ceramics 33.3 and 16.6 mmol g^{-1}, respectively. It was confirmed at long times, where the isothermal curves presented CO_2 absorptions as a function of their chemical capacity.

Similar isothermal data have been fitted to various kinetic models.[10,16,21,84,85,89,90] In general, simple (eqn (8)) or double (eqn (9)) exponential models have been used in order to elucidate the direct CO_2 capture (superficial reaction), and the CO_2 capture kinetically controlled by diffusion processes, which occurs once the external shell is formed.

$$Q = Ae^{-k_1 t} + C \quad (8)$$

$$Q = Ae^{-k_1 t} + Be^{-k_2 t} + C \quad (9)$$

where Q corresponds to the rate at which CO_2 is captured (weight increase); t is the time; and k_1 and k_2 are the exponential constants for the CO_2 directly captured over the lithium silicate particles and CO_2 captured kinetically controlled by diffusion processes, respectively. In Fig. 13 we show data (k_1 and k_2 values) together with fits of the integral of eqn (9) from 0 to t with fitted values for the constants A, B, k_1, k_2. The fitted rate constants k_1, k_2 differ significantly for each lithium silicate. Similar results have been obtained by others,[15,17,21,32,85,86,91–93] and it has been established that k_1 values are always, at least, one order of magnitude higher than those obtained for the k_2 constants, independently of the lithium ceramic. We associate the small k_2 rate constant with the slow diffusion processes of stage two of the capture mechanism as discussed at the beginning of this section.

Once the isotherms were fitted to the double exponential model, the following results were obtained. For Li_2O we found the highest k_1 value, but the smallest k_2 value. It means that Li_2O reacts very quickly with the particle surface, but once the diffusion processes are activated, CO_2 capture is very slow. The slow diffusion in Li_2O may arise because the external shell is composed of Li_2CO_3 in this case, whereas other lithium secondary phases are present in the external shell during CO_2 absorption by the other lithium silicates and may make faster diffusion possible, depending on temperature.[87]

Li_8SiO_6 presents a smaller k_1 value than that of Li_4SiO_4. However, we must take into account that Li_8SiO_6 presents a double consecutive reaction process producing Li_4SiO_4 as an initial intermediate, which may attenuate the superficial reaction, as it is evidenced in the corresponding Li_4SiO_4 isothermal curve. In contrast, the presence of the same Li_4SiO_4 as intermediate may increase the lithium ion diffusion, enhancing the k_2 value of the corresponding Li_8SiO_6.

Some of these kinetic data have been further analyzed by fitting the temperature dependence of the fitted rate constants using Arrhenius or Eyring models. Table 6 shows the experimental results reported for different lithium silicates. In each case, the corresponding activation energies (E_a from the Arrhenius model) or activation enthalpies ($\Delta H^{\neq}$ from the Eyring model) are reported.[10,15,17,21,32,85,86,91–93] It should be pointed out that none of these samples presented any kind of porosity, and their surfaces areas were ≤ 3.0 m^2 g^{-1}.

Table 6 The obtained activation enthalpy ($\Delta H^{\neq}$) or energy activation (E_a) values of the CO_2 capture on lithium silicates

Lithium silicates	Temperature range (°C)	Energy (kJ mol^{-1}) CO_2 direct	Diffusion control	Ref.
Li_2O	200–600	3.6[a]	—	10
Li_8SiO_6	500–700	48.1[b]	—	32
Li_4SiO_4	500–600	71.2[a]	83.4[a]	86
K-doped Li_4SiO_4	500–650	45.8[a]	60.1[a]	86
Na-doped Li_4SiO_4	500–650	56.6[b]	96.8[b]	85
Li_4SiO_4 (S_{BET}, 0.4 m^2 g^{-1})	460–650	94.4[b]	37.2[b]	16
Li_4SiO_4 (S_{BET}, 1.5 m^2 g^{-1})	460–650	83.4[b]	32.0[b]	16
Li_4SiO_4 (S_{BET}, 3.0 m^2 g^{-1})	500–650	88.9[b]	79.5[b]	85

[a] E_a value. [b] $\Delta H^{\neq}$ value.

According to the results listed in Table 6, it seems that there is not a general defined trend. While some results suggest that the CO_2 direct absorption process is more dependent on temperature than the CO_2 absorption controlled by diffusion processes, for other lithium silicates we find exactly the contrary. The variations observed between these results may arise in part from the fact that the temperature range over which the fit was done was not large and varied from one silicate to another. However, Li_8SiO_6 possesses smaller activation enthalpy than Li_4SiO_4, independently of the specific Li_4SiO_4 physicochemical characteristics, but larger than Li_2O (the reported value of Li_2O corresponds to E_a). In the Li_8SiO_6 case, the experimental results showed that Li_8SiO_6 reacts with CO_2 to produce Li_4SiO_4 over the external shell, which consequently reacts with more CO_2 (depending on temperature) to produce Li_2SiO_3. This reaction mechanism agrees with the theoretical results reported above. Finally, two other factors must be taken into account: (1) doped-lithium silicates present better CO_2 absorption capacities, and it has been associated with the eutectic phase formation.[11,13,18] (2) Surface area increments modified the CO_2 capture process as this whole process depends on the direct (related to the surface area) and diffusion control reactions (related to the bulk material).[16,87,92]

In addition, one of the major parameters for potential applications of these materials is related to the cyclability. Among these lithium silicates, there are a few cyclability reports related to Li_4SiO_4. Kato *et al.* reported efficiency cyclic performances up to 90% after 50 cycles using Li_4SiO_4 alone or mixed with other lithium ceramics.[94]

Obviously, in order to fully understand the mechanisms of their CO_2 capture process and evaluate their possible industrial applications further theoretical and experimental analyses of Li^+ and O^{2-} diffusion through the shell are needed and under investigation.

4.5.4 Synthesis of new lithium silicate materials by adjusting the Li_2O/SiO_2 ratio. As shown in Fig. 11, Li_2O is a strong CO_2 sorbent as it can absorb CO_2 over a wide range of P_{CO_2} at high temperatures.[45] However, it is not a good CO_2 sorbent because its reverse reaction to release CO_2 can happen only at much higher temperatures.[45,50] Meanwhile, as a very weak CO_2 sorbent, SiO_2 usually does not capture CO_2. As shown in Table 1, when going from Li_2O to various lithium silicates and further to SiO_2, the Li_2O/SiO_2 ratio decreases. Fig. 14 shows the relationship of the Li_2O/SiO_2 ratio (plotted as a function of SiO_2 molar percentage) with the turnover temperatures (T_1, T_2, T_1', T_2') and CO_2 capture capacities among various lithium silicates.

As shown in Fig. 14 and Table 5, by decreasing the Li_2O/SiO_2 ratio, the corresponding turnover temperatures (T_1 and T_2) and the CO_2 capture capacities of these lithium silicates also decreased. Such results indicate that by changing the Li_2O/SiO_2 ratio we can find and synthesize a lithium silicate with an

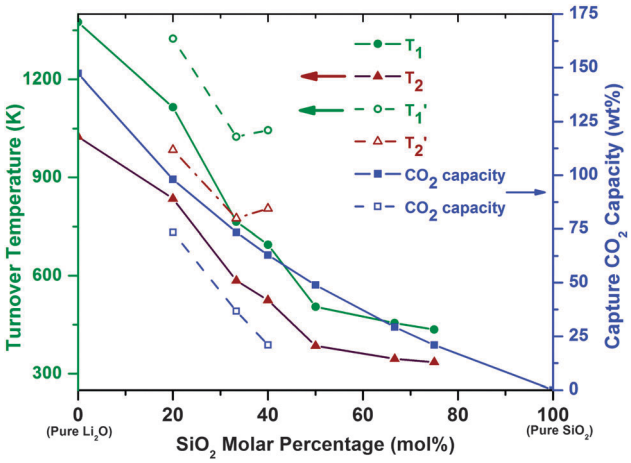

Fig. 14 The dependence of the turnover temperatures defined in the text and of CO_2 capture capacity on molar percentage of SiO_2 in the silicates for which calculations are reported here. T_1 and T_1' are the turnover temperatures under pre-combustion conditions with CO_2 partial pressure at 20 bars, while T_2 and T_2' are the turnover temperatures under post-combustion conditions with CO_2 partial pressure at 0.1 bar. The solid lines indicate conversion of lithium silicates into SiO_2 and Li_2CO_3 (T_1, T_2). For those Li_2O-rich lithium silicates (Li_8SiO_6, Li_4SiO_4, $Li_6Si_2O_7$) capturing CO_2, the data shown in dashed lines indicate their conversion into Li_2SiO_3 and Li_2CO_3 (T_1', T_2'). The corresponding CO_2 capture capacities are plotted using open blue squares.

operating temperature which falls into the range required for certain existing power plants because the regenerating temperature of pure Li_2O is too high to be used in practical CO_2 capture technologies.[45,50] In other words, even if one single material (*e.g.* Li_2O, SiO_2, *etc.*) may not be a good CO_2 sorbent to fit practical capture needs (certain ranges of P_{CO_2} and temperature), by mixing (or doping) two or more solids (*e.g.* $Li_2O + SiO_2$, $Li_2O + ZrO_2$, $MgO + Na_2O$, *etc.*) to form a new material (such as lithium silicates, lithium zirconates,[24,30,95] double salts,[96] *etc.*), the resulting material may satisfy the industrial requirements. Generally speaking, when we add more quantities of weak-sorbent (in our case SiO_2) into a strong sorbent (in our case Li_2O), the newly formed lithium silicate will have an overall lower CO_2 capture capacity and its turnover temperatures will shift to lower values compared to those obtained for the pure Li_2O as shown in Fig. 14. From this figure and the data in Table 5, the theoretical CO_2 weight percentage maxima of these lithium silicates are greater than 3 mmol per gram sorbent ($\sim$15 wt%). Therefore, all these systems satisfy the required criteria related to the minimum amount of CO_2 capture capacity, and only other issues could limit their applications as CO_2 sorbents.

Based on our results, when we mix two solids A and B to form a new sorbent C, the turnover temperature of the newly resulting system (T_C) is located between those of A and B (T_A, T_B). Here it was assumed that A is a strong CO_2 sorbent while B is a weak CO_2 sorbent and $T_A > T_B$. Also, we assumed that the desired operating temperature T_O is between T_A and T_B ($T_A > T_O > T_B$). Now, depending on the properties of A and B, we have typically three scenarios to synthesize the mixing sorbent C: (1) $T_A \gg T_B$ and the A component is the key part to capture CO_2. Our Li_2O–SiO_2 mixed lithium silicates belong to this category. Li_2O–ZrO_2 mixed lithium zirconates are also part of this category.[24,30,95] As discussed above, in this case, T_A is too high to be useful for CO_2 capture. After mixing A and B with adjusted A/B ratio, the T_C of the newly formed C compound could be close to the T_O temperature to fit the practical needs; (2) $T_A \gg T_B$ and B component is the key part to capture CO_2. In this case, since T_B is lower than T_O, mixing A with B will increase the turnover temperature T_C of the C solid to values closer to T_O. For example, pure MgO has a very high theoretical CO_2 capture capacity. However, its turnover temperature (250 °C) is lower than the required temperature range of 300–470 °C in warm gas clean up technology, and therefore, it cannot be directly used as a CO_2 sorbent in this technology. By mixing alkali metal oxides M_2O (M = Na, K, Cs) or carbonates (M_2CO_3) with MgO, the corresponding newly formed systems have higher turnover temperatures, making them useful as CO_2 sorbents through the reaction $MgO + CO_2 + M_2CO_3 = M_2Mg(CO_3)_2$;[96] (3) the T_A and T_B are close to each other. In this case, both A and B components are active to capture CO_2, and the CO_2 capacity of the mixture is the summation of those of A and B. As we know another potential advantage of mixing solids is to increase the surface area of the solids in order to have faster reaction rate. Such a mixing scenario doesn't show too much advantage in shifting the capture temperature, but may enhance the kinetics of the capture process and eventually make the mixtures more efficient. Although there is no such report in the literature, we think such an attempt is worthwhile. Our primary results for the class of lithium silicates can provide some general guidelines to design and synthesize new CO_2 sorbents and in such cases computational modeling can play a decisive role in identifying materials with optimal performance.

5. Summary and conclusions

By combining first-principles density functional theory with lattice phonon dynamics, we investigated the electronic and lattice dynamics properties of a series of lithium silicates with different Li_2O/SiO_2 ratios. Based on the calculated thermodynamic properties of these solids, we further explored their CO_2 capture properties.

The calculated band structures showed that these lithium silicates have larger band-gaps (>4.5 eV). By decreasing the Li_2O/SiO_2 ratio, the band gap and the VB_1 width of the corresponding lithium silicate increase. In all lithium silicates, the p orbitals of Li have a larger contribution than its s orbital and all of them are involved in forming all the VBs and CB. The p orbitals of O mainly contribute to VB_1 while its s orbital mainly contributes to VB_2. The upper portion of VB_1 is mainly due to the interactions between Li and O. Both the s and p orbitals of Si contribute to the lower portion of VB_1 and VB_2.

Based on the calculated phonon dispersions of these lithium silicates, we confirm the stability of the reported crystallographic structure in all but one case. The exception is $Li_6Si_2O_7$ for which the phonon analysis gave two branches of relaxation modes,

indicating the existence of an unstable structure. The instability in this case is associated with relaxation of Si–O tetrahedra in the *xy* plane and is under continuing investigation. By decreasing the Li_2O/SiO_2 ratio, the vibrational frequencies of the lithium silicates shift to high frequencies. The phonon free energies and entropies obtained from the phonon calculations on these lithium silicates are used to evaluate their thermo-stability, phase transformation, and CO_2 capture properties.

By mixing Li_2O with SiO_2 in different ratios, all of the resulting lithium silicates are favored thermodynamically to be formed. By adding SiO_2 to a Li_2O-rich lithium silicate, a Li_2O-poor lithium silicate could be obtained, and *vice versa*. It is also possible to convert a SiO_2-rich lithium silicate to one with a high Li_2O/SiO_2 ratio by adding Li_2O.

Based on the calculated thermodynamic data for lithium silicates, their CO_2 capture properties (such as the CO_2 capacity, the turnover temperatures, and the heat of reaction) were fully investigated. By increasing the Li_2O/SiO_2 ratio (from $Li_2Si_3O_7$ up to Li_8SiO_6), the corresponding lithium silicates were found to have higher CO_2 capture capacities, higher turnover temperatures, and higher heats of reaction. Obviously, the lithium silicate with higher Li_2O/SiO_2 ratio will require more energy input to be regenerated at higher temperature. For the Li_2O-rich lithium silicates (Li_8SiO_6, Li_4SiO_4, $Li_6Si_2O_7$), when the capture temperature is lower than the turnover temperature of Li_2SiO_3, they can absorb CO_2 to form Li_2CO_3 and SiO_2 with high CO_2 capture capacity. However, if the capture temperature is above the turnover temperature of Li_2SiO_3, the products will be Li_2CO_3 and Li_2SiO_3 with low CO_2 capture capacity. The SiO_2-rich lithium silicates ($Li_2Si_2O_5$, $Li_2Si_3O_7$) can thermodynamically absorb CO_2 at relatively low temperature with low capture capacity. However, if the temperature is too low, the kinetics of CO_2 capture reaction is too slow as demonstrated by the experiments reported here. Therefore, some tradeoff must be made.

By measuring the isotherms of CO_2 absorbed by lithium silicates, we concluded that the CO_2 capture of lithium silicates is a two-step process. In the first step, the lithium silicate particles react with CO_2 at the particle surface. This superficial reaction involves the formation of an external shell composed of lithium carbonate and a metal oxide or a lithium secondary phase, depending on the initial composition. Once the first stage is complete, the second step corresponding to the bulk diffusion processes must be activated for the silicates to continue CO_2 chemisorption. The second step generally requires an increase in temperature. Our results showed that the second stage corresponding to the bulk diffusion is the controlling step for the kinetics and for the CO_2 capture capacity.

By changing the mixing ratio of Li_2O and SiO_2, we can obtain different lithium silicate solids which exhibit different thermodynamic behaviors, such as heats of reaction and turnover temperatures. These results can be used to provide guidelines for designing new CO_2 sorbents. One single material taken in isolation might not be an optimal CO_2 sorbent to fit the particular needs to operate at specific temperature and pressure conditions. By mixing or doping two or more materials to form a new material, it is possible to synthesize new CO_2 sorbent formulations which can fit the industrial needs. For these purposes, we analyzed and discussed three scenarios for mixing different solid sorbents in an attempt to identify formulations with optimal performance for CO_2 capture applications.

Appendix

In a multi-phase system constructed by P phases with S species, the Gibbs free energy is extensive:[97]

$$G = \sum_{j=1}^{\mathrm{P}} G^{(j)} = \sum_{j=1}^{\mathrm{P}} \sum_{i=1}^{\mathrm{S}} \mu_i^{(j)} N_i^{(j)} \tag{A1}$$

where j labels phases, i labels species, $N_i^{(j)} = \chi_j n_j^i$.

In case only CO_2 is in the gas phase, then

$$G = \sum_{j}^{p-1} x_j F_j + x_{\mathrm{g}} \mu_{\mathrm{g}}^{\mathrm{CO_2}} n_{\mathrm{g}}^{\mathrm{c}} \tag{A2}$$

Because the reactions proceed at fixed gas pressure and temperature and at fixed chemical composition of the solids, the reaction thermodynamics are obtained by minimization of a 'grand canonical' free energy G' defined by

$$G' = G - \mu_{\mathrm{g}}^{\mathrm{CO_2}} N_{\mathrm{C}} \tag{A3}$$

where N_{c} is the total number of carbon atoms. Then since

$$x_{\mathrm{g}} n_{\mathrm{g}}^{\mathrm{c}} = N_{\mathrm{c}} - \sum_{j=1}^{p-1} x_j n_j^{\mathrm{c}} \tag{A4}$$

we rewrite G' as

$$G' = \sum_{j}^{p-1} x_j F_j - \mu_{\mathrm{g}}^{\mathrm{CO_2}} \sum_{j}^{p-1} x_j n_j^{\mathrm{c}} \tag{A5}$$

which is eqn (6).

Notes and references

1 D. Cruz, S. Bulbulian, E. Lima and H. Pfeiffer, *J. Solid State Chem.*, 2006, **179**, 909–916.
2 K. Essaki, M. Kato and K. Nakagawa, *J. Ceram. Soc. Jpn.*, 2006, **114**, 739–742.
3 K. Essaki, M. Kato and H. Uemoto, *J. Mater. Sci.*, 2005, **40**, 5017–5019.
4 K. Essaki, K. Nakagawa, M. Kato and H. Uemoto, *J. Chem. Eng. Jpn.*, 2004, **37**, 772–777.
5 C. Gauer and W. Heschel, *J. Mater. Sci.*, 2006, **41**, 2405–2409.
6 J. Ida, R. T. Xiong and Y. S. Lin, *Sep. Purif. Technol.*, 2004, **36**, 41–51.
7 M. Kato and K. Nakagawa, *J. Ceram. Soc. Jpn.*, 2001, **109**, 911–914.
8 M. Kato, S. Yoshikawa and K. Nakagawa, *J. Mater. Sci. Lett.*, 2002, **21**, 485–487.
9 A. Lopez-Ortiz, N. G. P. Rivera, A. R. Rojas and D. L. Gutierrez, *Sep. Sci. Technol.*, 2004, **39**, 3559–3572.
10 H. A. Mosqueda, C. Vazquez, P. Bosch and H. Pfeiffer, *Chem. Mater.*, 2006, **18**, 2307–2310.

11 B. N. Nair, R. P. Burwood, V. J. Goh, K. Nakagawa and T. Yamaguchi, *Prog. Mater. Sci.*, 2009, **54**, 511–541.
12 K. Nakagawa and T. Ohashi, *J. Electrochem. Soc.*, 1998, **145**, 1344–1346.
13 K. Nakagawa and T. Ohashi, *Electrochemistry*, 1999, **67**, 618–621.
14 T. Okumura, K. Enomoto, N. Togashi and K. Oh-ishi, *J. Ceram. Soc. Jpn.*, 2007, **115**, 491–497.
15 M. Olivares-Marin, T. C. Drage and M. M. Maroto-Valer, *Int. J. Greenhouse Gas Control*, 2010, **4**, 623–629.
16 R. Rodriguez-Mosqueda and H. Pfeiffer, *J. Phys. Chem. A*, 2010, **114**, 4535–4541.
17 M. J. Venegas, E. Fregaso-Israel, R. Escamilla and H. Pfeiffer, *Ind. Eng. Chem. Res.*, 2007, **46**, 2407–2412.
18 R. Xiong, J. Ida and Y. S. Lin, *Chem. Eng. Sci.*, 2003, **58**, 4377–4385.
19 T. Yamaguchi, T. Niitsuma, B. N. Nair and K. Nakagawa, *J. Membr. Sci.*, 2007, **294**, 16–21.
20 X. S. Yin, Q. H. Zhang and J. G. Yu, *Inorg. Chem.*, 2011, **50**, 2844–2850.
21 M. Seggiani, M. Puccini and S. Vitolo, *Int. J. Greenhouse Gas Control*, 2011, **5**, 741–748.
22 J. Ortiz-Landeros, C. Gomez-Yanez and H. Pfeiffer, *J. Solid State Chem.*, 2011, **184**, 2257–2262.
23 Y. Duan and K. Parlinski, *Phys. Rev. B: Condens. Matter Mater. Phys.*, 2011, **84**, 104113.
24 Y. Duan, *J. Renewable Sustainable Energy*, 2012, **4**, 013109.
25 B. Y. Li, Y. Duan, D. Luebke and B. Morreale, *Appl. Energy*, 2013, **102**, 1439–1447.
26 M. E. Bretado, V. G. Velderrain, D. L. Gutierrez, V. Collins-Martinez and A. L. Ortiz, *Catal. Today*, 2005, **107–108**, 863–867.
27 T. Okumura, Y. Matsukura, K. Gotou and K. Oh-Ishi, *J. Ceram. Soc. Jpn.*, 2008, **116**, 1283–1288.
28 Y. J. Wang, L. Qi and W. J. Jiang, *Chin. J. Inorg. Chem.*, 2006, **22**, 268–272.
29 M. D. Donne, E. Gunther, G. Schumacher, G. Sordon, D. Vollath, H. Wedemeyer and H. Werle, *J. Nucl. Mater.*, 1991, **179**, 796–799.
30 Y. Duan, *J. Renewable Sustainable Energy*, 2011, **3**, 013102.
31 J. Ortiz-Landeros, C. Gomez-Yanez, L. M. Palacios-Romero, E. Lima and H. Pfeiffer, *J. Phys. Chem. A*, 2012, **116**, 3163–3171.
32 F. Durán-Muñoz, I. C. Romero-Ibarra and H. Pfeiffer, *J. Mater. Chem. A*, 2013, **1**, 3919–3925.
33 H. Migge, *J. Nucl. Mater.*, 1988, **151**, 101–107.
34 D. Vollath and H. Wedemeyer, *J. Nucl. Mater.*, 1986, **143**, 334–338.
35 F. C. Kracek, *J. Phys. Chem.*, 1930, **34**, 2641–2650.
36 S. Claus, H. Kleykamp and W. SmykatzKloss, *J. Nucl. Mater.*, 1996, **230**, 8–11.
37 H. Kruger, V. Kahlenberg and R. Kaindl, *J. Solid State Chem.*, 2007, **180**, 922–928.
38 W. Y. Ching, Y. P. Li, B. W. Veal and D. J. Lam, *Phys. Rev. B: Condens. Matter Mater. Phys.*, 1985, **32**, 1203–1207.
39 T. Uchino and T. Yoko, *J. Phys. Chem. B*, 1999, **103**, 1854–1858.
40 T. Uchino and T. Yoko, *J. Phys. Chem. B*, 1998, **102**, 8372–8378.
41 K. Munakata and Y. Yokoyama, *J. Nucl. Sci. Technol.*, 2001, **38**, 915–918.
42 J. C. Du and L. R. Corrales, *J. Chem. Phys.*, 2006, **125**, 114702.
43 J. C. Du and L. R. Corrales, *J. Non-Cryst. Solids*, 2006, **352**, 3255–3269.
44 J. C. Du and L. R. Corrales, *J. Phys. Chem. B*, 2006, **110**, 22346–22352.
45 Y. Duan and D. C. Sorescu, *Phys. Rev. B: Condens. Matter Mater. Phys.*, 2009, **79**, 014301.
46 G. Kresse and J. Hafner, *Phys. Rev. B: Condens. Matter Mater. Phys.*, 1993, **47**, 558–561.
47 G. Kresse and J. Furthmuller, *Comput. Mater. Sci.*, 1996, **6**, 15–50.
48 Y. Duan, *Phys. Rev. B: Condens. Matter Mater. Phys.*, 2008, **77**, 045332.
49 Y. Duan and D. C. Sorescu, *J. Chem. Phys.*, 2010, **133**, 074508.
50 Y. Duan, B. Zhang, D. C. Sorescu and J. K. Johnson, *J. Solid State Chem.*, 2011, **184**, 304–311.
51 H. J. Monkhorst and J. D. Pack, *Phys. Rev. B: Solid State*, 1976, **13**, 5188–5192.
52 C. J. Bradley and A. P. Cracknell, *The mathematical theory of symmetry in solids*, Clarendon press, Oxford, 1972.
53 S. Cristol, J. F. Paul, E. Payen, D. Bougeard, S. Clemendot and F. Hutschka, *J. Phys. Chem. B*, 2002, **106**, 5659–5667.
54 Y. Duan, D. Luebke and H. W. Pennline, *Int. J. Clean Coal Energy*, 2012, **1**, 1–11.
55 B. Zhang, Y. Duan and J. K. Johnson, *J. Chem. Phys.*, 2012, **136**, 064516.
56 M. W. J. Chase, *J. Phys. Chem. Ref. Data*, 1998, **9**, 1–1951.
57 A. R. Akbarzadeh, V. Ozolins and C. Wolverton, *Adv. Mater.*, 2007, **19**, 3233–3239.
58 V. Ozolins, E. H. Majzoub and C. Wolverton, *J. Am. Chem. Soc.*, 2009, **131**, 230–237.
59 R. B. Darst, *Introduction to linear programming: applications and extensions*, Marcel Dekker Inc., New York, 1991.
60 R. Hofmann and R. Hoppe, *Z. Anorg. Allg. Chem.*, 1987, **555**, 118–128.
61 H. Vollenkl, A. Wittman and H. Nowotny, *Monatsh. Chem.*, 1969, **100**, 295–303.
62 K. F. Hesse, *Acta Crystallogr., Sect. B: Struct. Crystallogr. Cryst. Chem.*, 1977, **33**, 901–902.
63 H. Voellenkle, *Z. Kristallogr.*, 1981, **154**, 77–81.
64 F. Liebau, *Acta Crystallogr.*, 1961, **14**, 389–395.
65 R. I. Smith, R. A. Howie, A. R. West, A. Aragonpina and M. E. Villafuertecastreion, *Acta Crystallogr., Sect. C: Cryst. Struct. Commun.*, 1990, **46**, 363–365.
66 S. Hull, T. W. D. Farley, W. Hayes and M. T. Hutchings, *J. Nucl. Mater.*, 1988, **160**, 125–134.
67 Y. Idemoto, J. W. Richardson, N. Koura, S. Kohara and C. K. Loong, *J. Phys. Chem. Solids*, 1998, **59**, 363–376.
68 N. R. Keskar and J. R. Chelikowsky, *Phys. Rev. B: Condens. Matter Mater. Phys.*, 1992, **46**, 1–13.
69 M. Ledyastuti, Y. F. Liang, C. R. Miranda and T. Matsuoka, *J. Chem. Phys.*, 2012, **137**, 034703.

70 J. R. Chelikowsky, N. Troullier, J. L. Martins and H. E. King, Jr., *Phys. Rev. B: Condens. Matter Mater. Phys.*, 1991, **44**, 489–497.
71 T. Demuth, Y. Jeanvoine, J. Hafner and J. G. Angyan, *J. Phys.: Condens. Matter*, 1999, **11**, 3833–3874.
72 G. A. Lager, J. D. Jorgensen and F. J. Rotella, *J. Appl. Phys.*, 1982, **53**, 6751–6756.
73 B. H. W. S. Dejong, D. Ellerbroek and A. L. Spek, *Acta Crystallogr., Sect. B: Struct. Sci.*, 1994, **50**, 511–518.
74 F. D. Murnaghan, *Am. J. Math.*, 1937, **59**, 235–260.
75 F. Birch, *Phys. Rev.*, 1947, **71**, 809–824.
76 HSC Chemistry software 6.1, Pori: Outotec Research Oy, www.outotec.com/hsc, 2006.
77 E. Gnani, S. Reggiani, R. Colle and M. Rudan, *IEEE Trans. Electron Devices*, 2000, **47**, 1795–1803.
78 N. Choudhury and S. L. Chaplot, *Phys. Rev. B: Condens. Matter Mater. Phys.*, 2006, **73**, 094304.
79 B. Dorner, H. Grimm and H. Rzany, *J. Phys. C: Solid State Phys.*, 1980, **13**, 6607–6612.
80 M. D. Donne, A. Goraieb, G. Piazza and G. Sordon, *Fusion Eng. Des.*, 2000, **49**, 513–519.
81 R. B. Khomane, B. K. Sharma, S. Saha and B. D. Kulkarni, *Chem. Eng. Sci.*, 2006, **61**, 3415–3418.
82 M. L. Gray, K. J. Champagne, D. Fauth, J. P. Baltrus and H. Pennline, *Int. J. Greenhouse Gas Control*, 2008, **2**, 3–8.
83 DOE-NETL, ''Cost and Performance Baseline for Fossil Energy Plants'', Volume 1: Bituminous Coal and Natural Gas to Electricity Final Report, http://www.netl.doe.gov/energy-analyses/baseline_studies.html, 2007.
84 Z. Qi, H. Daying, L. Yang, Y. Qian and Z. Zibin, *AIChE J.*, 2013, **59**, 901–911.
85 V. L. Mejia-Trejo, E. Fregoso-Israel and H. Pfeiffer, *Chem. Mater.*, 2008, **20**, 7171–7176.
86 K. Wang, X. Guo, P. F. Zhao, F. Z. Wang and C. G. Zheng, *J. Hazard. Mater.*, 2011, **189**, 301–307.
87 J. Ortiz-Landeros, T. L. Avalos-Rendon, C. Gomez-Yanez and H. Pfeiffer, *J. Therm. Anal. Calorim.*, 2012, **108**, 647–655.
88 L. Martinez-dlCruz and H. Pfeiffer, *J. Phys. Chem. C*, 2012, **116**, 9675–9680.
89 I. Alcerreca-Corte, E. Fregoso-Israel and H. Pfeiffer, *J. Phys. Chem. C*, 2008, **112**, 6520–6525.
90 T. Avalos-Rendon, V. H. Lara and H. Pfeiffer, *Ind. Eng. Chem. Res.*, 2012, **51**, 2622–2630.
91 T. Avalos-Rendon, J. Casa-Madrid and H. Pfeiffer, *J. Phys. Chem. A*, 2009, **113**, 6919–6923.
92 L. Martinez-dlCruz and H. Pfeiffer, *Ind. Eng. Chem. Res.*, 2010, **49**, 9038–9042.
93 X. S. Yin, M. A. Song, Q. H. Zhang and J. G. Yu, *Ind. Eng. Chem. Res.*, 2010, **49**, 6593–6598.
94 M. Kato, K. Nakagawa, K. Essaki, Y. Maezawa, S. Takeda, R. Kogo and Y. Hagiwara, *Int. J. Appl. Ceram. Technol.*, 2005, **2**, 467–475.
95 Y. Duan, *Phys. Chem. Chem. Phys.*, 2013, **15**, 9752–9760.
96 K. Zhang, X. S. Li, Y. Duan, P. Singh, D. L. King and L. Li, *Int. J. Greenhouse Gas Control*, 2013, **12**, 351–358.
97 J. W. Halley, *Statistical Mechanics_From first principles to macroscopic phenomena*, Cambridge University Press, New York, 2007.

